Algorithm Theoretical Basis Document

for

ASTER Level 2B1 - Surface Radiance
and
ASTER Level 2B5 - Surface Reflectance

Principal Investigator: Kurt Thome
Contract Number: NAS5-31717

Contributions by Stuart Biggar and Tsutomu Takashima

Remote Sensing Group

of the

Optical Sciences Center

University of Arizona
Tucson, Arizona 85721

March 30, 1999

Table of Contents

1.0 INTRODUCTION

1.1 Algorithm Identification and Data Product

This Algorithm Theoretical Basis Document (ATBD) describes the algorithm for the Level 2B1 and 2B5 products for the Advanced Spaceborne Thermal Emission and Reflectance Radiometer (ASTER) which is a sensor on NASA's Earth Observing System (EOS) AM-1 platform. The Level 2B1 product is surface radiance and the Level 2B5 product is surface reflectance. We refer to this process as the atmospheric correction of ASTER data. Both algorithms are described in the same document because they are closely related and require similar input data sets using the same look-up table (LUT) approach. The document discusses the atmospheric correction of visible and near-infrared (VNIR) and shortwave-infrared (SWIR) data only. The atmospheric correction for the thermal-infrared (TIR) part of the spectrum is discussed in a closely related document.

1.2 Algorithm Overview

The atmospheric correction for the VNIR and SWIR is based upon a LUT approach using results from a Gauss-Seidel iteration radiative transfer code (RTC) (Herman and Browning, 1965). The method has its basis in the reflectance-based, vicarious-calibration approach of the Remote Sensing Group at the University of Arizona (Slater et al., 1987). We are applying the knowledge learned from our calibration methods to the atmospheric correction of the VNIR and SWIR bands for ASTER. Specifically, the RTC we have used for the past 10 years is used as a basis for a look-up-table approach to atmospheric correction. The method currently assumes atmospheric scattering optical depths and aerosol parameters are known from outside sources. Using these parameters, a set of piecewise-linear fits are determined from the LUT that relate the measured satellite radiances to surface radiance and surface reflectance.

1.3 Document Scope

This document concentrates on the algorithm for the Version 1 atmospheric correction which will be used for computer sizing requirements and for testing outside data dependencies. The document limits itself to describing the algorithm. Plans for implementing the algorithm are not discussed here. The ATBD is related to and part of a package of documents used to describe the conversion of the algorithm to production code. The purpose of this document is to allow the ASTER team leader to make informed decisions regarding the use and implementation of the algorithm and indicate areas which may be problematic in implementation.

Other documents as part of this package include the Software Management Plan, the Standard Data Product Specification, Software Requirements Document, the Test Plan, and the Science Computing Facilities document. These documents describe how the code will be developed from the algorithm and the hardware for which the code is being developed.

1.4 Document Organization

The ATBD first describes the overall algorithm in detail. Background information and overview are given including the experimental objective of the algorithm, an historical perspective, and instrument characteristics of interest.

This algorithm description is from a theoretical standpoint with discussions of the physical basis of the problem, mathematical solution, and an estimate of the variance or uncertainty. As part of the algorithm description there is a discussion of practical considerations for implementation of the algorithm. The last section covers limitations, constraints, and assumptions.

2.0 OVERVIEW AND BACKGROUND INFORMATION

This section has three parts. The first gives the experimental objective. The second section gives an historical perspective of the algorithm. The last part describes the instrument characteristics important to this algorithm.

2.1 Experimental Objective

The experimental objective of the algorithm is to correct the ASTER TOA radiance for the effects of atmospheric scattering and absorption in the VNIR and SWIR portions of the spectrum. Accurate atmospheric correction can remove the effects of changes in satellite-sun geometry and atmospheric conditions (Teillet, 1991). Atmospherically corrected surface reflectance images improve the accuracy of surface type classification (Fraser et al., 1977, and Kaufman, 1985) and are also a basis for estimating the radiation budget of the Earth (Kimes and Sellers, 1985). Full use of satellite data for agricultural resource management also requires atmospheric correction (Moran et al., 1990).

2.2 Historical Perspective

The atmospheric correction described in this ATBD is based on the calibration and related atmospheric correction work of the Remote Sensing Group (RSG) of the Optical Sciences Center at the University of Arizona. Our calibration work uses the reflectance-based method which has been used since the mid-1980s to radiometrically calibrate Systeme Pour l'Observation de la Terre (SPOT) -1, -2, and -3 (Begni et al., 1986, Gellman et al., 1993) and Landsat-4 and -5 Thematic Mapper (TM) (Slater et al., 1987, and Thome et al., 1993). The method relies on ground-based measurements of the surface and atmosphere at a selected site to predict top-of-the-atmosphere (TOA) radiances. (Slater et al., 1987). Surface measurements are made for a number of pixels by transporting spectroradiometers across a test site and measuring upwelling radiance. This radiance is converted to reflectance by comparing it with measurements from a panel of known reflectance. Solar radiometer data are converted to atmospheric transmittances (Gellman et al., 1991) and used to determine the aerosol properties and columnar absorber amounts over the site (Biggar et al., 1990, Thome et al., 1992). The results are used as input to a RTC to predict the TOA radiance. The digital

numbers (DNs) reported by the sensor are compared to these predicted radiances to give a radiometric calibration.

The RTC used in our calibration work has also been used as part of an atmospheric correction scheme implemented by the RSG (Holm et al., 1989). Here, the ground-based solar radiometers are still used to characterize the atmosphere in a similar fashion. The derived atmospheric parameters are used as input to the RTC for several assumed values of the surface reflectance. Although the relation between surface reflectance and TOA radiance is quadratic over the full 0-1 range of reflectance (Slater and Jackson, 1982), over shorter ranges the relation is sufficiently linear that an assumption of linearity causes negligible error. The code radiance output is calculated for two reflectance values. These radiances and the satellite radiances derived from the image DNs are matched by linear interpolation, and the corresponding reflectance factor value obtained. An example of this near-linear relationship is shown in Figure 1.

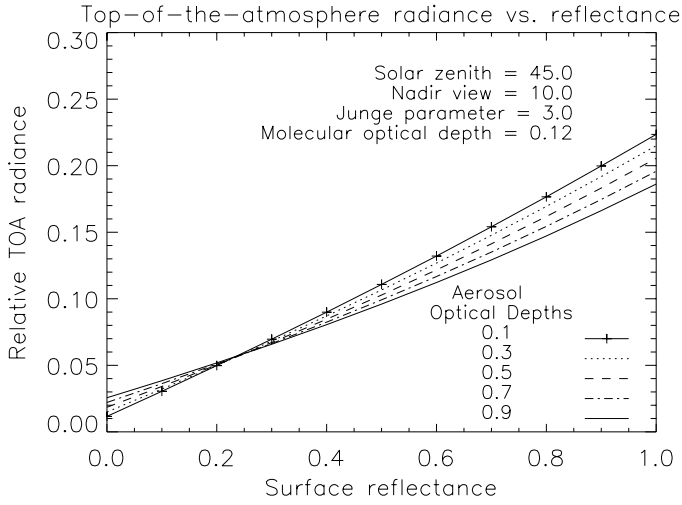

Figure 1 Radiative transfer code output illustrating near-linear relationship between surface radiance and TOA radiance.

Application of this approach to TM imagery yielded uncertainties of 0.008 in reflectance over an agricultural area with reflectance ranging from 0.02-0.55 (Holm et al., 1989). Application to HRV data resulted in retrievals of reflectance to better than 10% absolute error for the same agricultural area with a 0.1-0.4 reflectance range (Moran et al., 1990). This study included off-nadir viewing angles similar to those expected from ASTER. A study of several atmospheric correction methods yielded better than a 0.015 RMS error in reflectance over the range of 0.02-0.63 for an approach similar to Holm et al., 1989 (Moran et al., 1992). This same study also showed that RSG's approach compares favorably with other atmospheric correction methods.

The above technique has only been used on sub-scenes on the order of 512×512 pixels. It has never been used operationally because running the full RTC for an entire image would be too computationally intensive. Even using approximate RTCs would be too intensive. LUTs can be used to save time and avoid the complexities of maintaining an RTC in an operational environment (Teillet, 1992). LUT approaches have been used successfully over water for CZCS (Fraser, 1993) and AVHRR (Stowe 1993) and over land for FIFE (Fraser et al., 1992). All three of these examples are based on similar RTCs to the one intended for use in this atmospheric correction.

2.3 Instrument Characteristics

ASTER is a high-spatial resolution imager scheduled to fly in Earth orbit in mid-1998, on the EOS-AM1 platform (Kahle et al., 1991 and Yamaguchi et al., 1993). The instrument consists of three subsystems: VNIR subsystem provided by NEC with 15-m resolution; SWIR subsystem provided by MELCO with 30-m resolution; and TIR subsystem provided by Fujitsu with 90-m resolution. The bands are centered at approximately 0.56, 0.66, and 0.81 μm for the VNIR subsystem (with bandpasses of 0.08, 0.06, and 0.10 μm respectively); 1.65, 2.165, 2.205, 2.26, 2.330, 2.395 μm for the SWIR (with bandpasses of 0.10, 0.04, 0.04, 0.05, 0.07, and 0.07 μm); and 8.30, 8.65, 9.10, 10.60, 11.30 μm for the TIR (with bandpasses of 0.35, 0.35, 0.35, 0.70, and 0.70 μm). The swath width for the three systems is 60 km, with crosstrack pointing of 8.6 degrees for the SWIR and TIR and 24.0 degrees for the VNIR subsystem. This ensures every point on earth is imaged once every 16 days by the SWIR and TIR and five days by the VNIR.

This atmospheric correction is applied only to the VNIR and SWIR bands. A separate algorithm is being developed for the TIR bands. The data used by this algorithm should be radiometrically corrected. Geometric correction will be necessary to incorporate digital elevation model (DEM) data and the atmospheric data from other sensors.

3.0 ALGORITHM DESCRIPTION

This section has two parts. The first part is a theoretical discussion of the algorithm including a description of the physics of the problem, a mathematical discussion of the algorithm, and a sensitivity analysis. The second part of this section covers practical considerations of implementing the algorithm, including a discussion of validation plans. Also included in this second section are planned methods of quality control, a discussion of data dependencies, and a description of the output product.

3.1 Theoretical Description

3.1.1 Physics of Problem

The physical basis of this problem relies on deriving a relationship between the surface radiance/reflectance and the TOA radiance from information regarding the scattering and absorbing characteristics of the atmosphere. This relationship is used to convert radiances measured by ASTER to surface radiance and reflectance. The ultimate problems are to determine the scattering and absorbing properties of the atmosphere and to find the relationship between surface reflectance/radiance and TOA radiance.

In the first two versions of the operational code, the absorbing and scattering characteristics of the atmosphere are planned to be obtained from outside sources. The anticipated sources of this information are results from other AM-1 platform sensors such as the Multi-Angle Imaging Spectroradiometer (MISR) and the Moderate-Resolution Imaging Spectroradiometer (MODIS). We

also anticipate using global assimilation model (GAM) results. Difficulties arise when these sources of information are not available. In these first two versions of the code, climatological data will be used when no atmospheric information are provided. Later versions, the first of which is expected to be delivered six to nine months after the launch of EOS-AM1, will offer the user an opportunity to perform an ASTER-only correction. A proposed approach for this ASTER-only correction is described later.

The relationship between surface radiance/reflectance to the TOA radiance is determined from radiative transfer calculations stored in a look-up table. This assumes that, given the absorbing and scattering properties of the atmosphere, we can model the way in which solar radiation is scattered or absorbed. Thermal emission is not considered by this algorithm because in the VNIR and SWIR it is negligible. We assume the earth is flat with a homogeneous, lambertian surface because difficulties are encountered in modeling the way radiation interacts with the earth-atmosphere system when inhomogeneities are present. The atmosphere is composed of plane-parallel, homogeneous layers. Obviously, this is not the case in nearly all real-world applications, but to attempt to completely address these problems leads to RTCs which are too computationally intensive for an operational approach or require look-up tables that are prohibitively large. Of course, approximate methods exist which can partly account for these effects and these methods will be included in later versions of the atmospheric correction.

3.1.2 Mathematical Description of Algorithm

3.1.2.a Radiative transfer code

The atmospheric correction algorithm is based on the relationship between the angular distribution of radiance, scattering and absorption in the atmosphere, and the surface properties. This relationship is described by the radiative transfer equation,

$$L_\lambda(s,\omega) = L_\lambda(0,\omega)\exp(-\delta(0, s)) + \int_0^s J_\lambda(s',\omega)\exp(-\delta_\lambda(s', s))d\delta_\lambda \quad \textbf{(1)}$$

where $L_\lambda(s,\omega)$ is the monochromatic radiance at the point s in the atmosphere in the direction ω at the wavelength λ. $L_\lambda(0,\omega)$ is the monochromatic radiance at the top or bottom of the atmosphere in the direction ω, and $\delta_\lambda(s',s)$ is the monochromatic optical depth along the path s' to s given by

$$\delta_\lambda(s', s) = \int_{s'}^{s} K_{\lambda T}(s')ds' \quad \textbf{(2)}$$

where $K_{\lambda T}(s')$ is the total volume extinction coefficient. The source function for a scattering-only atmosphere, $J_\lambda(s',\omega)$, is written

$$J_\lambda(s',\omega) = P_\lambda(\omega,\omega_0)E_\lambda(s',\omega_0) + \frac{1}{4\pi}\int_0^{4\pi} P_\lambda(\omega,\omega')L_\lambda(s',\omega')d\omega' \qquad \textbf{(3)}$$

where $P_\lambda(\omega,\omega')$ is the phase function describing the angular distribution of particle scattering, and $E_\lambda(s',\omega_0)$ is the monochromatic, solar irradiance at the point s′ in the solar direction, ω_0.

Because the radiance distribution appears on both sides of (1), no analytical solution exists, but (1) can be solved numerically by dividing a model atmosphere into homogeneous, plane-parallel layers based upon the total optical thickness of the atmosphere. The horizontal distribution of scatterers is assumed to be homogeneous and their vertical distribution follows that of a modified 1976 U. S. Standard Atmosphere. The modification arises to allow for a separate phase function to be incorporated for stratospheric aerosols. The surface is assumed to be horizontally homogeneous in reflectance but it can be non-lambertian. The downwelling radiance at the top of the atmosphere is assumed to be zero. Aerosols in the atmosphere are assumed to be spherical and behave as Mie scatterers and molecules are assumed to be Rayleigh particles.

Solving for the radiance distribution begins by computing what is termed the single scatter component using the first term on the RHS of (3) and integrating by path length using (1). In practice, the path length integral is approximated by a summation over the discrete layers composing the model atmosphere. Single scatter radiances are found for each level for a discrete set of directions. These directions are every 10 degrees in zenith (5, 15, 25, ..., 155, 165, 175) and every 30 degrees in azimuth (0, 30, 60, 90, 120, 150, and 180). The code accepts arbitrary solar angles as input. The phase function that is computed is an average value determined for the solar input direction into an output wedge of directions. For example, to compute the phase function related to the solar beam being scattered to the zenith direction of 15 degrees and the azimuth direction of 60 degrees, a wedge corresponding to zenith angles of 10 to 20 and azimuths of 45 to 75 degrees is created. The scattering phase function is computed at one degree intervals in both azimuth and zenith within this wedge and averaged.

The single scatter radiances serve as the first guess to the Gauss-Seidel iteration. Beginning at the top of the atmosphere, the iteration begins by solving (1) numerically for the first discrete direction ω. The updated value for radiance in this direction is then used in subsequent calculations to obtain the radiance in the second direction. This is repeated until new values of radiances have been calculated for all directions at the first level. The method then proceeds to the second level and repeats the process of iterating through all of the directions. This is done for all layers in the atmosphere moving downward one level at each step. When the bottom of the atmosphere is reached, the surface reflectance, ρ, is used to compute the upward traveling incident radiance. If E_{down} is the total downwelling irradiance at the surface and we assume the surface is lambertian, then the reflected radiance is $\rho E_{down}/\pi$. These radiances are used in the calculations as the method proceeds upward through the atmosphere. This downward-upward process is repeated until the radiances change

<0.1% from one pass to the next and the angular distribution of radiance is known throughout the atmosphere at each of the discrete directions.

This radiance field is used to determine the radiance at the top of the atmosphere for the given arbitrary view directions using one last pass upward through the atmosphere. In this case, the process begins by computing the average phase functions in a similar fashion to that of the single scatter case. Here, the average phase function is computed for the specific output view direction and the wedge of angles as the input. The upwelling radiance in the direction of interest is computed using the directional reflectance and the downwelling irradiance. Equation (1) is then solved for each layer using the desired direction as the output direction and integrating over the discrete set of angles used to compute the entire radiance field.

The input parameters for the radiative transfer code include solar and view zenith angle and surface reflectance. Other inputs describe atmospheric properties, including molecular and aerosol scattering optical depths, aerosol index of refraction, and aerosol size distribution. The code handles ozone absorption but strong absorption by water vapor must be treated separately.

3.1.2.b Look-up-table approach

The above described RTC is very efficient computationally. Even so, it is not feasible to use the code itself to perform the atmospheric correction of ASTER data. A conservative estimate for the number of runs of the RTC to do the atmospheric correction is 25 per band. This corresponds to a total of more than 1500 runs for the VNIR and SWIR bands of ASTER when the multiple surface reflectances are considered. On a Sparc20 machine, this translates to nearly a day to simply perform the radiative transfer calculations for a typical set of atmospheric conditions and range of surface reflectances. A more approximate RTC that is more computationally efficient would still take on the order of hours to compute the necessary radiances, but at the expense of accuracy. Thus, we need either much faster computers (several orders of magnitude faster), fewer runs of the RTC, or a look-up table. It was decided to use the look-up table because it gives us an efficient means to solve the problem without sacrificing too much accuracy.

The RTC described above is used to generate the LUT used for the atmospheric correction. The LUT is based on the following parameters: solar zenith angle, satellite view angle, relative azimuth angle between the satellite and sun, molecular scattering optical depth, aerosol scattering optical depth, aerosol single scatter albedo, aerosol size distribution parameter, and surface reflectance. The size distributions that are used are based either on a Junge size distribution (or power law) or are based on the set of aerosol types used to develop the atmospheric correction for MISR.

The Junge-based distributions are useful because they allow the size distribution to be described with one parameter. This simplifies the look-up procedures and reduces the size of and the time to generate the LUT. If, for instance, a log-normal distribution were used, two parameters would be required to generate and use the table. This doubles the size of the table as well as doubles the time required to generate the table. Single scatter albedo incorporates the complex index of refraction for

the aerosol particles. Elevation changes are treated as changes in the molecular and aerosol optical depths to again simplify the table and the look-up procedures.

3.1.2.c Reflectance vs. Radiance

The actual atmospheric correction is the process of retrieving the surface radiance and surface reflectance from the satellite radiances. To do this, the scattering and absorbing properties of the atmosphere are determined using techniques described in the next section. Columnar amounts of absorbing gases are used to compute the sun-to-surface-to-satellite gaseous transmittance. The satellite radiances are divided by these transmittances to determine a satellite radiance for an atmosphere which does not contain gaseous absorption. The scattering optical depths, single scatter albedo, and size distribution are used along with the solar and view angles to determine the appropriate portion of the LUT to use.

In most cases, the values of the input parameters to the atmospheric correction will not match those used to generate the LUT. In these cases, there are several methods which could be used to determine the set of at-satellite radiances, surface radiances, and surface reflectances to be retrieved from the table. For the current work, a combination of interpolation and nearest-neighbor approaches will be used. The advantage to interpolation schemes is that the size of the table may be reduced. However, this is at the cost of increasing the complexity of the LUT scheme. If a nearest-neighbor approach is used, the resolution of the table parameters must be selected so that the use of the table is not a primary source of error. Thus, the LUT access is simplified, but the size of the table, and time needed to generate it, could become prohibitively large. By using a combined approach, we can optimize the size of the table while still maintaining satisfactory accuracy.

However, for Version 1, we have adopted a nearest-case approach. This allows the code developers to test computational requirements of the code. It should be emphasized that the Version 2 code will use a combination of nearest-neighbor and interpolation.

Once the appropriate surface radiances, reflectances, and TOA radiances have been determined from the table, piecewise-linear fits are calculated between the TOA radiance and the surface reflectance. Similar fits are also found between the TOA radiance and the surface radiance. The ASTER scene radiance is then used with the proper linear fit to determine the surface radiance and reflectance.

3.1.2.d LUT Resolution

The goal of selecting the parameters that will be used to generate the LUT is to develop the smallest table possible while still producing accurate results. The reasons for wanting a small LUT are it takes less time to generate and requires less computer storage. A study of the sensitivity of the TOA radiances to LUT parameters was done to determine what values should be used to generate the table. The study approaches the problem from two viewpoints. The first is to examine the percent difference in radiances for two runs of the RTC. The runs are nearly-identical except for changes in one of the input parameters. The differences found in this fashion show what errors could be expected if the ASTER data being atmospherically corrected relied on matching the actual case to the

nearest LUT case. The goal is to generate a LUT which contributes <3% to the determination of radiance at the top of the atmosphere for a given set of input parameters. As will be seen in the section discussing uncertainties, this will keep the LUT from being a dominant source of uncertainty in the problem.

Another approach, which requires more effort to develop and a greater number of clock cycles to implement is interpolation between LUT cases to the actual case being corrected. In all discussions below, it should be kept in mind that there is a direct tradeoff between LUT size and interpolation requirements. Each of the input parameters are considered separately with each section having a summary of recommended values/intervals.

It should be pointed out that in the following discussion we refer to intervals and differences in the parameters being examined. This interval is related to the difference between the value of the parameter that would be used to generate the LUT and the value of the parameter for a given ASTER pixel. Thus, when the interval for the work described below is 0.2, this means that the resolution of the LUT would be 0.4, or twice the difference listed in the following sections. This is because the largest difference between the scene value and LUT value will be one-half the interval used to generate the LUT.

Wavelength: Based on the results of numerous RTC runs, it can be concluded that only two wavelengths are required to generate the LUT, one for the VNIR and one for the SWIR. The one for the VNIR would use the wavelength for band 2 (660 nm) and the one in the SWIR would use band 5 (2205 nm). Changes in wavelength have only two effects on the radiative transfer. The first is a change in the scattering phase function. This is a small effect when compared to changes in the phase function imposed by uncertainty in the Junge parameter and index of refraction. The second effect is that single scatter albedo itself is wavelength dependent. That is, for a given aerosol index of refraction, the single scatter albedo changes slightly with wavelength. Thus, if the single scatter albedo is known for each band, the wavelength effect can be partially corrected.

Figures 2, 3, and 4 help illustrate these effects. Figure 2 shows the percent change in the scattering phase function between the upper and lower wavelengths of both the VNIR and SWIR telescopes computed using a Junge parameter of 3.0, real index of refraction of 1.44, and imaginary index of 0.03. This figure represents one a severe

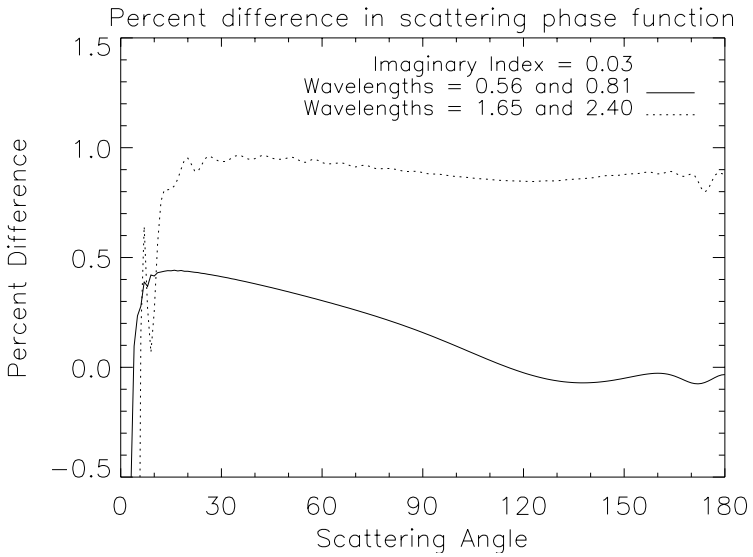

Figure 2. Percent difference in Mie scattering phase function computed for the upper and lower wavelengths of VNIR and SWIR telescopes.

case, yet still shows phase function differences <1% for scattering angles between the solar beam and the view angles of ASTER. The larger effects at other scattering angles are mitigated by multiple scattering.

Figures 3 and 4 show the percent change in TOA radiance between two wavelengths as a function of surface reflectance when the scattering optical depths are held constant. In these figures, the aerosol optical depths were assumed to be 0.8. The effects seen here are similar for other optical depths. Some of the percent difference can be attributed to the difference in single scatter albedo. For instance, the VNIR case in Figure 3 shows a percent difference of 2% for an imaginary index of 0.03. At 0.56 μm the single scatter albedo is 0.723 while at 0.81 μm the single scatter albedo is 0.715. This accounts for about 0.5% of the difference in the radiance. By selecting the middle wavelength for each spectral region and adjusting for imaginary index effects, the percent error from using only one wavelength should be in the 0.5-1.0% range.

The above results are valid when a Junge-based aerosol size distribution is used and the absorption can be controlled by altering the imaginary index of refraction. For the case of matching the aerosol size distributions used by the MISR team, use of a single wavelength is not adequate in all cases. Thus, for the MISR-type aerosols, we will generate LUT results for all three ASTER VNIR bands. A single wavelength will still be used for the SWIR bands because the uncertainty due to extrapolating the aerosol effects from the four MISR bands that are in the VNIR to the SWIR bands of ASTER is expected to be larger than the effects of changes in the aerosol properties across the SWIR spectral region.

Reflectance interval: For this parameter, only the interpolation differences were examined because the atmospheric correction relies on interpolating the TOA radiance versus reflectance to do the actual correction. Values of 0.0, 0.1, 0.2, 0.3, 0.5, 0.7, and 1.0 have been selected. If quadratic interpolation is adopted, the number of required reflectances would be further reduced. This reduces the time required to generate the LUT but increases the number of accesses required and this increases the time it takes to do the atmospheric correction.

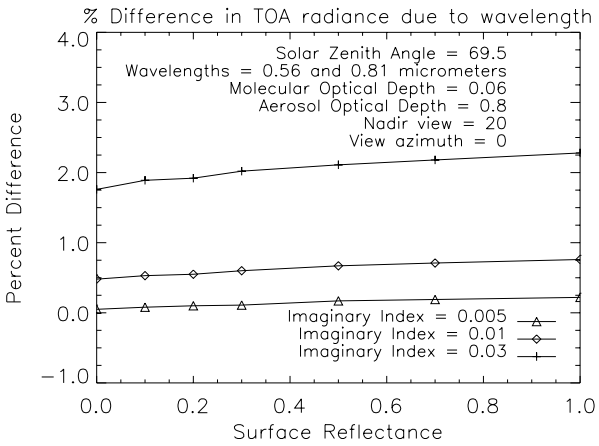

Figure 3. Percent difference for VNIR TOA radiances due to wavelength differences.

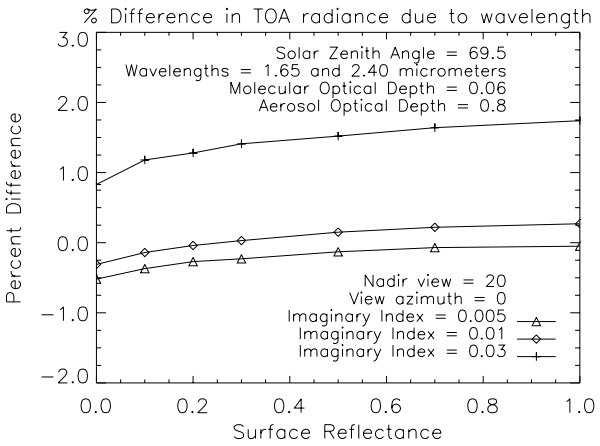

Figure 4. Percent difference for SWIR TOA radiances due to wavelength differences.

View azimuth effects: The effect due to azimuth angle was examined using 15-degree differences. For reflectances greater than 0.3, a 15 degree interval is acceptable. At reflectances less than 0.3 a smaller difference is required when the view zenith is greater than 10 degrees. For view zenith <10 degrees, a difference of less than 15 degrees is not required except for reflectances less than 0.2.

Figures 5 and 6 illustrate some of these effects. Figure 5 shows the percent difference due to a 15 degree change in azimuth angle for the conditions listed in the graph. The feature to notice in this figure is that the uncertainty for a surface reflectance of 0.05 is nearly one-half the value for a reflectance of 0.0. The uncertainty becomes much smaller as the reflectance continues to increase. Figure 6 is similar to Figure 5, except two different optical depths are shown as well as the results for a different solar zenith. This shows both the dependency on scattering optical depth and on the scattering phase function.

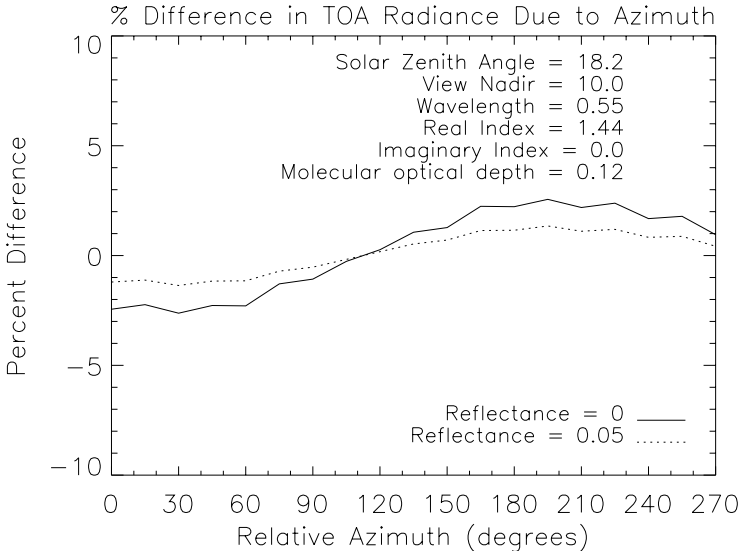

Figure 5. Percent difference in TOA radiance due to 15 degree uncertainty in relative azimuth.

It still might be acceptable to have larger than 1% TOA radiance differences at low reflectances because at these reflectances a large percent difference does not translate into a large absolute difference in retrieved reflectance. This needs to be examined further. An additional point is that using a linear interpolation scheme does not reduce the required azimuth interval because the shape of the radiance versus azimuth curves are sharply peaked.

The values that have been selected are 0 to 180 degrees at 15 degree intervals for reflectances larger than 0.1. Thus, the largest difference between a LUT value of azimuth and a scene value will be 7.5 degrees. An interval of 7.5 degrees has been selected for reflectances of 0.0 and 0.1.

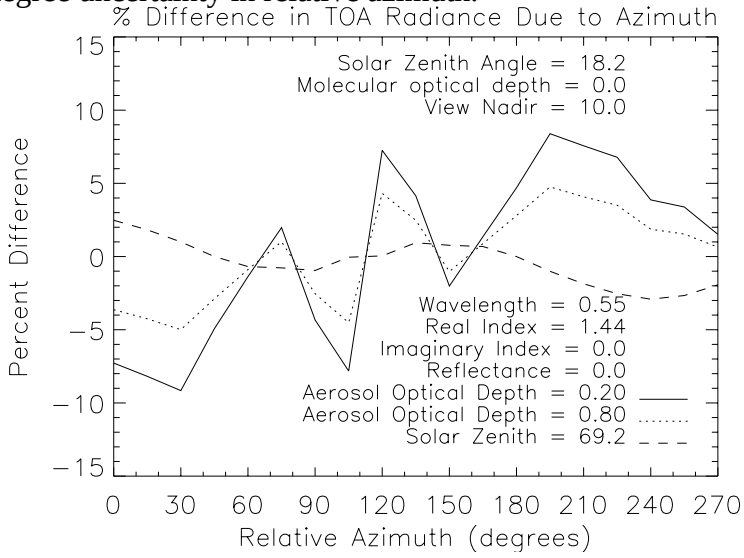

Figure 6. Percent difference in TOA radiance due to 15 degree uncertainty in relative azimuth.

View zenith angle: Work done in this study indicate the difference between view angles can be larger for smaller views and must be smaller for larger view angles. In no case, should the difference between the LUT value and the scene value exceed 2 degrees, unless the interval is tailored for specific situations. For example, a larger interval would be possible for higher surface reflectances, with a low solar zenith angle, and low scattering optical depth. The interval could be further increased if interpolation is done. The number of view angles required to handle the SWIR case is much fewer than for the VNIR because the SWIR telescope only points to about 8 degrees off-nadir. The angles that have been selected are at two-degree intervals for 0 to 10 degrees and at one-degree intervals for view angles larger than 10 degrees. For the SWIR, this means only five angles are used.

Junge parameter: As with most of the parameters, the effect due to changing Junge parameter is larger at lower reflectance. Changes of 0.25 in Junge parameter were found to give differences larger than 1% for all cases where the surface reflectance was less than 0.2 and for most cases when the surface reflectance was less than 0.5. Interpolation greatly reduces the difference in all cases to the point that a 0.5 difference in Junge parameter between the LUT value and the scene value is acceptable. Figures 7 and 8 illustrate these points. Figure 7 shows the percent difference in the radiance due to a 0.25 change in the Junge parameter for the conditions shown and surface reflectances of 0.0 and 0.1. Figure 8 shows the dependency of the uncertainty for different view angles. This shows that the effect is caused primarily by differences in determining the phase function.

Another issue which has been examined is the likelihood of some Junge parameter values. For instance, the theoretical upper limit for the parameter is 6.0 which corresponds to aerosols that are the same size as air molecules. This is extremely unlikely, but still possible. It should be reasonable, though, to accept larger errors in these

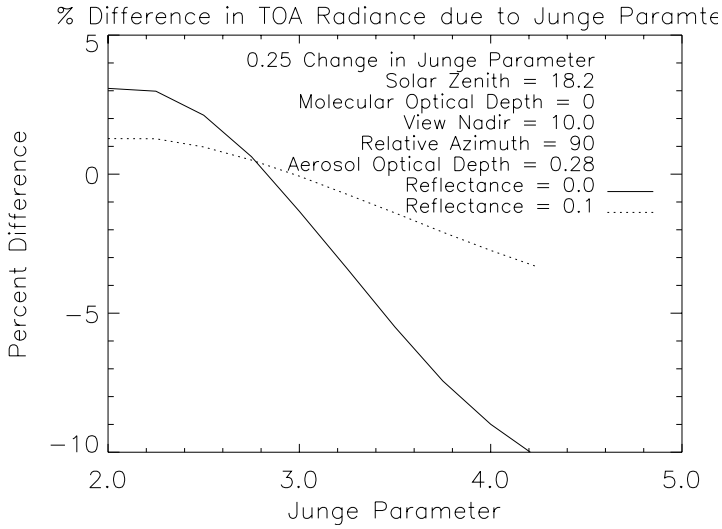

Figure 7. Percent difference in TOA radiance due to a 0.25 difference in Junge parameter.

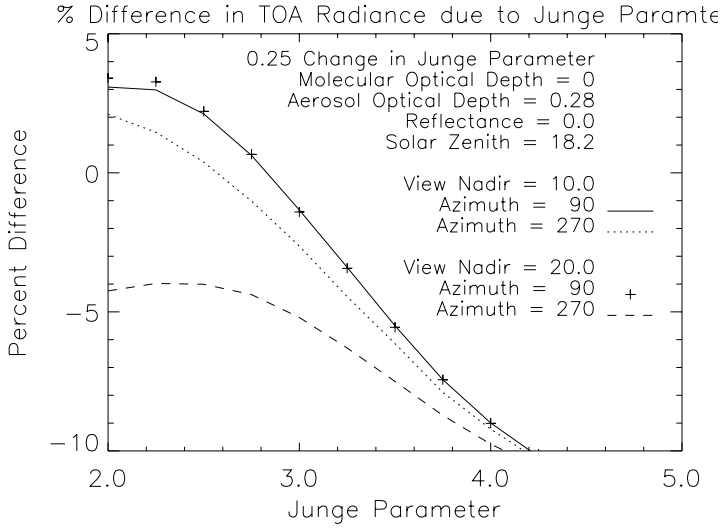

Figure 8. Percent difference in TOA radiance due to a 0.25 difference in Junge parameter.

unlikely cases as a tradeoff for reducing LUT size to improve efficiency for the much larger number of "normal" cases. Finally, the lower limit for the Junge parameter needs to be examined. The limit used currently is 2.0 but there is no theoretical lower limit, except that imposed by gravitational fallout of larger particles. The current table is based on Junge size distributions with 6 values (2.0, 2.5, 3.0, 3.5, 4.0, and 4.5) coupled with interpolation.

Solar Zenith Angle: This work examined the effect on TOA radiance due to changing the solar zenith angle by 0.01 in cosine of the angle. That is, the cosine of the solar zenith at 0 degrees is 1.00. The next solar zenith angle used was 8.1 degrees for which the cosine is 0.99. The radiances were computed for solar zenith from 0 to 70 degrees at the 0.01 cosine interval. In all cases, the differences between runs was greater than 1% and much larger for backscatter situations. Differences are much smaller when interpolation is used and in all cases, except for backscatter situations, the cosine interval can exceed 0.05 and still have less than a 1% difference between the actual and interpolated values.

It should be obvious that it is unrealistic to use a cosine interval of 0.01. This leads to 66 values for solar zenith angle to cover the range from 0 to 70 degrees. Thus, the current approach will be to use interpolation techniques to account for the variation of this parameter and we plan to use 14 values for solar zenith angles ranging from 0 to 70 degrees at 0.05 intervals in cosine. Work is still being done to determine the optimal method for handling solar zenith angles larger than 70 degrees. This will be complicated by the fact that at larger solar zenith angles the assumption of the earth-atmosphere system being plane-parallel begins to break down.

Aerosol Optical depth: The study showed the effect of aerosol optical depth resolution is larger for smaller reflectance cases. If the zero reflectance case is ignored, differences are less than 1% for differences in aerosol optical depth of 0.025. Larger than 1% differences occur at surface reflectance of 0.0. If interpolation is used, the change in radiance is less than 0.3% for a 0.15 interval in optical depth. The maximum value for aerosol optical depth still needs to be determined. Values in excess of 1.00 are extremely unlikely and these cases would suffer from larger errors regardless of the optical depth interval used. The current proposal is to use 7 values, 0.0 to 0.9 at 0.15 intervals with an interpolation scheme.

Molecular Optical depth: The results of studies of this parameter are essentially identical to those for aerosol optical depth. If the zero reflectance case is ignored, differences are less than 1% for differences in molecular optical depth of 0.025. If interpolation is used, the difference in radiance is less than 0.3% for a 0.15 interval in optical depth. This covers the entire range of expected molecular optical depths for ASTER since the maximum expected value for molecular optical depth is around 0.12 for band 1 at a high surface pressure. The maximum expected value for the SWIR is less than 0.002 for band 4 which is the shortest wavelength band in the SWIR. The current plan is to use 3 values of molecular optical depth, 0.01 to 0.13 at 0.06 intervals for the VNIR and 1 value of 0.002 for the SWIR bands.

Index of refraction: The most likely driver of what values will be used for real index will be the expected values from MISR, MODIS, and climatology for each telescope. For a Junge aerosol

distribution and 0.1 intervals in real index, the differences are much larger than 1%. This is reduced to less than 1% for interpolation cases. The imaginary index is related to the single scatter albedo and thus the absorption by aerosol particles. In this study, we used imaginary index values from 0 to 0.1 at 0.005 intervals. These intervals gave differences greater than 2% for all cases. Interpolation reduced the differences to less than 1% for imaginary index intervals of up to 0.01.

To overcome some of the problems with determining an index of refraction interval, we have opted to develop the table based on typical real and imaginary index pairs (d'Almeida et al., 1991). Climatological values indicate that 26 different real and imaginary cases are needed for the VNIR and 20 for the SWIR. The values selected for the VNIR are:
[(1.39, 0.0000), (1.40, 0.0000), (1.52, 0.0100), (1.52, 0.0150), (1.53, 0.0012), (1.53, 0.0040)
(1.53, 0.0045), (1.53, 0.0050), (1.53, 0.0055), (1.53, 0.0060), (1.53, 0.0070), (1.53, 0.0078)
(1.53, 0.0085), (1.53, 0.0350), (1.53, 0.0400), (1.54, 0.0320), (1.54, 0.0330), (1.54, 0.0340)
(1.61, 0.1820), (1.61, 0.1870), (1.62, 0.1800), (1.62, 0.1810), (1.62, 0.1820), (1.62, 0.1840)
(1.62, 0.1880)]
and for the SWIR, the cases are:
[(1.18, 0.0034), (1.27, 0.0020), (1.32, 0.0107), (1.36, 0.0019), (1.37, 0.0007), (1.37, 0.0018)
(1.38, 0.0007), (1.42, 0.0014), (1.42, 0.0120), (1.42, 0.0175), (1.42, 0.0225), (1.42, 0.0800)
(1.44, 0.0420), (1.44, 0.0450), (1.44, 0.0490), (1.44, 0.1050), (1.57, 0.2020)
(1.59, 0.2070), (1.59, 0.2160)]

MISR aerosol parameters: In addition to developing the LUT with a set of Junge-based aerosol size distributions, we are developing a LUT that uses aerosol types corresponding to those being used in the MISR atmospheric correction. The planned MISR aerosol types include 95 different non-cloud, aerosol mixtures that, when coupled with the spectral bands, required means a total of 285 and 95 aerosol cases for the MISR types for the VNIR and SWIR respectively. For the Junge size distributions, there are 156 and 120 aerosol cases for the VNIR and SWIR respectively.

Summary of LUT parameters: The above results for the LUT are summarized in Tables 1 and 2 for the VNIR and SWIR respectively. If test output of the radiative transfer code are used with the numbers listed, the LUT would have a total size of approximately 3.0 GBytes in ASCII form. However, the use of the database format for the LUT causes this size to be dramatically reduced, and the overall size of the entire table is expected to be less than 3 Gbytes.

3.1.2.e Atmospheric scattering and absorbing properties

As has been mentioned previously, the number and type of scattering and absorbing properties will be obtained from outside sources whenever possible. The reasons for this are 1) the ASTER wavelengths were not selected for atmospheric remote sensing, 2) atmospheric sensors (MISR and MODIS) are on the same platform as ASTER, and 3) it will ensure that an atmospheric correction product will be ready at launch. The above should not be construed to imply that no ASTER-only atmospheric correction approaches will be attempted. This is elaborated in the next section. The discussion of this section assumes the atmospheric properties are available from an outside source.

Table I
Number of values required to generate the VNIR LUT for the atmospheric correction.

Reflectance	7
Relative azimuth	13
View zenith	20
Solar Zenith	14
Aerosol optical depth	7
Molecular optical depth	3
Junge aerosol cases	156
MISR aerosol cases	285
Total Cases	235,970,280

Table II
Number of values required to generate the SWIR LUT for the atmospheric correction.

Reflectance	7
Relative azimuth	13
View zenith	5
Solar Zenith	14
Aerosol optical depth	7
Molecular optical depth	1
Junge aerosol cases	120
MISR aerosol cases	95
Total Cases	9,586,850

Because several of the ASTER bands are sensitive to gaseous absorption, it is necessary to obtain the columnar amounts for absorbing gases. The transmittance is computed using a modified form of the program MODTRAN for the ASTER spectral responsivities determined during preflight calibration. These transmittances are computed for the sun-to-surface-to-satellite path and are used to correct the ASTER radiances.

It is expected that information about the scattering properties of the atmosphere will be available in a wide variety of formats. The following describes how these different inputs will be converted to size distribution, single scatter albedo at the ASTER wavelengths, and scattering optical depths at the ASTER wavelengths.

The simplest atmospheric parameter to derive is the molecular scattering optical depth. If we assume air molecules approximate Rayleigh scatterers, the molecular scattering optical depth depends only upon the atmospheric pressure (from the number of molecules) and wavelength,

$$\delta_r(\lambda) = \sigma_s(\lambda) \int_{z_0}^{z_t} N(z) dz \ , \qquad \textbf{(4)}$$

where N(z) is the number density of molecules as a function of height, z_0 is the ground elevation, and z_t is the height of the top of the atmosphere. The scattering cross-section for unpolarized light, $\sigma_s(\lambda)$, can be written as

$$\sigma_s(\lambda) = \frac{8\pi^3(m_r^2 - 1)^2}{3\lambda^4 N_s^2} \frac{6 + 3\rho}{6 - 7\rho} . \quad \textbf{(5)}$$

In this case, ρ is an anisotropy factor of 0.0279 (Young, 1981), m_r is the real part of the complex refractive index of the molecules and is close to unity, but wavelength dependent. N_s is the number of molecules per unit volume. As can be seen from (4) and (5), we can calculate $\delta_r(\lambda)$ from the number of molecules, N_s, obtained from the atmospheric pressure.

All of the other atmospheric parameters are related to the atmospheric aerosols. Ideally, these parameters would be given in a fashion that exactly matches values used in the LUT for the bands of ASTER. This will not be the case for most situations, thus it is necessary to convert the input data to parameters of this format. In all cases we assume the aerosol scattering phase function can be computed assuming Mie scattering (Bohren and Huffman, 1983).

If the only available information are spectral aerosol scattering optical depths, these data are used to determine a Junge aerosol size distribution. The aerosol size distribution is then used to determine scattering optical depths at ASTER wavelengths. The Junge distribution may be written as

$$\frac{dn(a)}{da} = C(z)a^{-(\nu+1)} \quad \textbf{(6)}$$

where a is the radius, n(a) is the number density, ν is the Junge parameter, and C(z) is a factor proportional to the aerosol concentration which is dependent on the height z. If we assume limits on the radius of 0 and ∞, we can show the aerosol optical depth may be written as

$$\delta_a(\lambda) = k\lambda^{-\nu+2} , \quad \textbf{(7)}$$

where

$$k = \pi(2\pi)^{\nu-2} \int_{z_0}^{z_t} C(z)dz \int_0^{\infty} \frac{Q_e(x)}{x^{\nu-1}} dx \quad \textbf{(8)}$$

$Q_e(x)$ is the extinction efficiency computed from Mie theory, and x is the size parameter defined as $x=2\pi a/\lambda$. If the limits of integration for the particle size are not 0 and ∞, k is not independent of wavelength. From (7), we can see $\log(\delta_a(\lambda))$ versus $\log(\lambda)$ gives a straight line. By fitting a straight line through all given aerosol optical depths using a weighted least-squares technique based on the

estimated error for each optical depth we can determine the Junge parameter (Biggar et al., 1990). Now we have an analytic expression for the aerosol optical depth as a function of wavelength based on the derived Junge parameter, and we can compute optical depths we need for use in our atmospheric correction for any sensor wavelength within the range of our measurements.

If the aerosol size distribution is available (in an arbitrary form) as well as an aerosol scattering optical depth for at least one wavelength, the aerosol scattering optical depth at ASTER wavelengths can be determined from Mie theory. The last parameter needed for the atmospheric correction is the single scatter albedo at ASTER wavelengths. The current approach for converting single scatter albedos at non-ASTER wavelengths to those at ASTER wavelengths will rely on climatological data.

3.1.2.f Atmospheric correction in the absence of atmospheric data

Currently, the atmospheric correction relies on aerosol information, either size distribution or spectral optical depths, from sources outside the ASTER data stream. If no concurrent aerosol information is available, the algorithm will rely upon climatological values determined as a function of location. In we have investigated other methods to be used for cases where no outside data are present. There are currently two basic methodologies being considered. The first of these is to determine the needed aerosol parameters for the LUT approach directly from ASTER data. The second approach is to develop an alternative approach which does not use the LUT. In this case, atmospheric properties are never explicitly determined. The problem with these approaches has already been alluded to in a previous section, ASTER bands were not selected for the purpose of determining atmospheric characteristics. ASTER does, however, have the advantage of having high spatial resolution and several bands in the SWIR.

One approach for in-scene atmospheric correction is using ground targets of known reflectance. Because of ASTER's high, ground-spatial resolution, this is easier than for sensors with larger ground footprints. We will attempt to implement an approach similar to that proposed by the MODIS atmospheric group. In this approach, SWIR data are used to determine areas of low reflectance due to dark vegetation or water. These areas correspond to areas of low reflectance in the VNIR which can then be used to determine the aerosol properties (Kaufman and Sendra, 1988). For MODIS, it has been proposed that bands at 3.9 and 2.1 μm will be used to determine the reflectance at 0.47 and 0.66 μm. ASTER does not have a band at 3.9 μm, but has several possible bands in the SWIR which can be used. Research must still be done to determine the relationship between the reflectance in the ASTER SWIR bands and those in the VNIR. The primary disadvantage to using ASTER data to determine aerosol properties is the lack of a band in the blue portion of the spectrum.

Two types of aerosol LUTs can be developed to handle the ASTER-only atmospheric correction. The first would be a LUT which uses the VNIR radiances over dark targets to determine the aerosol properties needed to access the appropriate part of the large atmospheric correction LUT used for the atmospheric correction approach described in a previous section. The second type of aerosol LUT would use the dark target radiances to define a set of reflectance/radiance curves for each band of ASTER and then directly retrieve the surface reflectance and radiance from these reflectance/radiance pairs. This approach avoids accessing the large atmospheric correction LUT. Both techniques will

be investigated and one will be selected to be implemented in a post-launch upgrade of the atmospheric correction code.

3.1.2.g Adjacency effect

Because of ASTER's high spatial resolution, it will be necessary to correct for adjacency effects to obtain accurate results. The approach that is planned is similar to that developed by Richter (1990) where a low pass filter is used to calculate the reflectance in the neighborhood or background of a selected pixel. This reflectance is used with the pixel reflectance to determine the amount of correction needed using a set of precomputed values. The advantage this method has is the number of pixels used in computing the background reflectance can be adjusted to make the approach more computationally efficient. Of course, if too few pixels are used, the results will be less accurate.

Tanre et al. (1981) investigated the adjacency effect for lambertian surfaces where the radiance at the top of the atmosphere is expressed by a sum of the radiative interactions between the atmosphere and the surface. The approach used an average reflectance of the environment and interactions for a maximum of six terms were considered with remaining, higher-order terms not exceeding 10 to 15% of the total contribution. Takashima and Masuda (1996) considered nine terms with a surface that was assumed to be lambertian. This work shows that the adjacency effect depends on the scene contrast, the sensor's spatial resolution, and the optical properties of the atmosphere. Because it is largest for high-spatial resolution sensors, large atmospheric scattering optical thicknesses, and high-contrast scenes, it should be clear that the adjacency effect must be taken into account to properly determine the surface reflectance and radiance for ASTER.

The adjacency effect is due to atmospheric scattering, and thus depends on the observation direction, incident solar direction, and atmospheric conditions. For the model presented here, we assume a plane-parallel, stratified atmosphere where the scatterers are constant within a layer. If the surface reflectance is spatially varying, the reflection function for the earth-atmosphere system can be expressed in a form consistent for use in a doubling-adding radiative transfer code

$$S_R(\delta) = S(\delta) + \frac{[\exp(-\delta/\mu)+T(\delta)]R_s(A,v_{wind})}{1-S(\delta)R_s(A,v_{wind})}[\exp(-\delta/\mu_0)+T(\delta)] \qquad \textbf{9}$$

where $S_R(\delta)$ provides the energy at the sensor for an optical thickness of δ (Takashima and Masuda, 1992). S and T are the reflection and transmission functions of the atmosphere, μ and μ_0 are the cosine of the view and solar zenith angles, A is the surface albedo, v_{wind} is the surface wind speed, and R_s is the surface reflection function. The denominator in this equation indicates an infinite series of hemispherical radiative interactions between the surface and the atmosphere. Including the first nine of these interactions for cases with the optical thickness less than 2.0 is enough to ensure uncertainties less than 1% (Takashima and Masuda, 1992).

Because the multiply-scattered energy from areas adjacent to the target is difficult to derive, we divide this process into three parts. First, the radiation from the target pixel is scattered diffusely through the atmosphere within the instantaneous field of view (IFOV), or equivalently, this is the forward-scattered energy from the surface. Second, radiation is scattered from within the sensor's IFOV outside the IFOV and back into the IFOV by atmospheric constituents. This can be viewed primarily as energy reflected from the surface scattered out of the sensor's IFOV and then scattered back into the IFOV by the atmosphere. Third, radiation reflected by adjacent pixels is scattered into the IFOV. The contribution of the first part is large because of the strong forward scattering by aerosol; the second and third parts are relatively small. Also, as the distance from the target pixel increases, the optical thickness of the slant path from the adjacent pixel to the sensor IFOV becomes larger and the contribution of the adjacent pixel to the target pixel decreases because the attenuation becomes larger.

Because of the assumptions made in our model, the ratio of the diffusely transmitted radiation from the adjacent pixel to that from the target pixel and the value of the diffusely transmitted radiation within the IFOV should be the same as that computed for single scattering. This assumption emphasizes the relative position of each respective pixel to the target rather than the precise radiative transfer processes in the atmosphere. The ratio, of course, decreases with increasing distance from the target, since the attenuation of the transmitted diffuse radiation increases with the distance. Accuracy may be improved if the interaction of radiation in and out of the IFOV is considered for the second and higher ordered scattering. Once a contribution is derived, multiple scattering in the atmosphere is considered in the IFOV for interactions of radiation between the atmosphere and pixels. Let $T_{a\text{-}i}$ be the singly-scattered diffuse radiation through the atmosphere that has been reflected from the i-th adjacent pixel. Similarly, let T_t be that from the target pixel and T_{prl} denote the value from a one-dimensional, atmosphere-surface system. If we define $a_i=T_{a\text{-}i}/T_t$., $\alpha_i=Ta\text{-}i/T_{prl}$, and $c=\Sigma\alpha_i$. Then $c=(T_t+\Sigma T_{a\text{-}1})/T_{prl}$. We use the parameter c to deduce the accuracy of our adjacency effect modeling since it should have a value of 1.0 for the best accuracy. It is also possible to determine the value of c for the homogeneous surface using the present simulation technique. Similarly we can also define a parameter β_i that is that same as α_i except for the case of diffuse reflection processes.

For a given set of atmospheric conditions and surface reflectance, it is possible to compute α_i and β_i as part of the LUT. Because this correction is for use in an operational environment, application of the adjacency correction will be limited to those cases where the surface heterogeneity causes the adjacency effect to cause a change in retrieved surface reflectance of 3% at reflectances greater than 0.2 and 0.006 reflectance units for low reflectance. As will be seen in the section on uncertainties, this applies the adjacency correction to cases where the uncertainty caused by ignoring the adjacency effect would exceed the uncertainties due to the use of a LUT.

Ideally, we would like to include all contributions from all pixels to determine the correction for adjacency effects for ASTER. However, this is simply not feasible in an operational method. If the contribution of the width of 20 km is considered, the total number of adjacent pixels becomes 2666 x 2666 for the case of the VNIR subsystem of ASTER. Therefore, substantial computation time would be required if all of these pixels were considered. Thus, a checkerboard size will be selected based on the distance between the target and adjacent pixels to reduce this computation time. Preliminary work indicates that adequate results can be obtained with as few as 441 pixels for

heterogeneous cases (and as few as 25 pixels in some situations). One other problem that we will have to deal with in performing an adjacency correction is that accurate profile data of the scatterers cannot be provided for ASTER data. Therefore we will adopt an equivalent height, where the optical properties equal those of an homogeneous atmosphere is introduced for the runs that are used to generate the adjacency correction LUT.

3.1.3 Variance/Uncertainty Estimates

For simplicity, the discussion of uncertainties is broken into two parts. The first part discusses the sensitivity in the TOA radiance to the input parameters for the LUT. This work is very closely related to the results presented previously for the LUT resolution study. The second part then relates the uncertainty in the TOA radiance to an uncertainty in retrieved surface reflectance. Throughout this discussion, the TOA radiances have been computed using the same Gauss-Seidel RTC which will be used to generate the LUT.

Table 3 lists the error sources we have identified for the atmospheric correction for cases where the surface reflectance is less than 0.1. Table 4 is the same as Table 3 except it is for cases where the surface reflectance is greater than 0.1. The reason for dividing the discussion into low and high reflectance is that many of the uncertainties depend strongly on reflectance. The error column is the error in the quantity listed in the source column. The source column values should be viewed as those which might be expected for this work, but post-launch validation will be required to determine their actual values. The total error column is the error in TOA radiance in percent caused by the item in the source column. The total is the root sum of squares of all the error sources. The choice of the root sum of squares is not necessarily valid as the sources are not known to be independent.

These tables are not meant to give the expected uncertainty in the retrieved reflectance from the atmospheric correction of ASTER. Rather, it is intended to indicate what parameters might cause problems when the atmospheric correction is implemented. A discussion of how these values were obtained follows.

3.1.3.a Sensor calibration

The first source of uncertainty to discuss is the sensor calibration. This is related to the error in converting the satellite digital numbers to radiance. The specification for ASTER is that this value is 4% absolute. In creating the summary tables, this value was assumed to be the same for both low and high values of reflectance, although this will most likely not be the case.

Table III

Uncertainty in TOA radiance determined from RTC runs for the listed sources. This case presents results for the low reflectance case.

Source	Error	Total Error
Sensor radiometric calibration	4%	4%
Scattering optical depth	0.05	8%
Single scatter albedo	0.01	5%
Junge size distribution parameter	0.5	10%
Surface height	100 m	4%
LUT		3%
Inherent code accuracy		1%
Total Error (root sum of squares)		15%

Table IV

Uncertainty in TOA radiance determined from RTC runs for the listed sources. This case presents results for the high reflectance case.

Source	Error	Total Error
Sensor radiometric calibration	4%	4%
Scattering optical depth	0.05	1%
Single scatter albedo	0.01	5%
Junge size distribution parameter	0.5	2%
Surface height	100 m	1%
LUT		3%
Inherent code accuracy		1%
Total Error (root sum of squares)		8%

3.1.3.b Scattering optical depth

Another source of uncertainty is determining the scattering optical depths at the ASTER wavelengths. To examine this uncertainty, we performed numerous runs of the RTC to examine the sensitivity in TOA radiance to changes in aerosol optical depth. The solar zenith was selected to be 45 degrees, a satellite view angle of 10 degrees, a relative azimuth of 150 degrees, a molecular scattering optical depth of 0.121, and a real index of refraction of 1.44. The aerosol size distribution was defined by a Junge parameter of 3.00. The imaginary index was 0.005 which yielded a single scatter albedo of 0.93. These parameters were then held constant while the aerosol scattering optical depth was varied from 0.0 to 1.0 at 0.025 increments and surface reflectance was varied from 0.0 to 1.0 at 0.1 increments.

The output of the runs was used to compute percent differences in TOA radiance for 0.025 and 0.05 changes in optical depth. The results of this are given in Figures 9 and 10. Figure 9 shows the percent change in TOA radiance as a function of optical depth for several surface reflectance values and an 0.025 change in optical depth. Figure 10 is the same except here the optical depth change is

0.05. From the figures it can be seen that the sensitivity to optical depth is strongly dependent upon the surface reflectance at low surface reflectances. When the surface reflectance exceeds 0.1 it can be seen that TOA radiance changes by less than 1% for optical depth uncertainties of 0.05. When the surface reflectance is less than 0.1, the uncertainty in TOA radiance can be as large as 8% for an optical depth uncertainty of 0.05.

3.1.3.c Imaginary index

The next source of uncertainty listed in the table is that due to the complex index of refraction (or single scatter albedo). To examine the effects due to this parameter RTC runs were performed using the case described above as the base case and using values for the complex index of 0.000, 0.0025, 0.005, 0.0075, and 0.010. The computed single scatter albedos for these runs were 1.00, 0.96, 0.93, 0.90, and 0.88, respectively.

Figure 11 shows the resulting percent difference in TOA radiance as a function of optical depth and surface reflectance using the cases for imaginary indexes of 0.0025 and 0.005. From the figure it is apparent that the uncertainty in TOA radiance is more strongly dependent upon the optical depth than on surface reflectance. Figure 12 shows the uncertainty in TOA radiance for an 0.0025 change in imaginary index for each of the values of imaginary index listed above as a function of optical depth. From this figure it can be seen that TOA radiance is more sensitive to changes in complex index for low values of index and high values of optical depth. Assuming that we can determine the single scatter albedo to better than 0.01 (about 0.0015 in complex index), the error due to this parameter should be less than 5%.

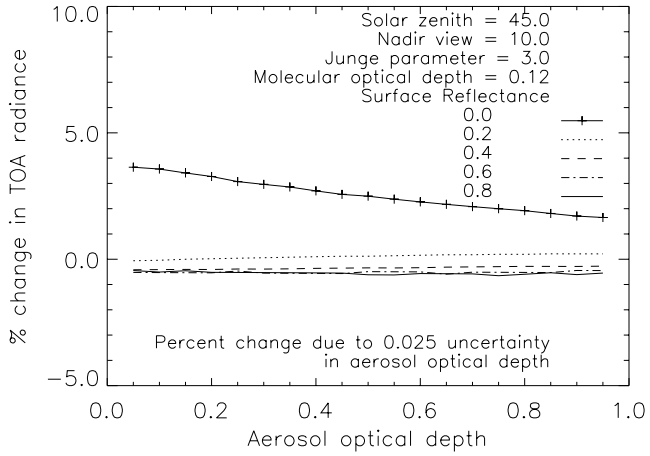

Figure 9 Uncertainty in TOA radiance due to an 0.025 change in aerosol scattering optical depth

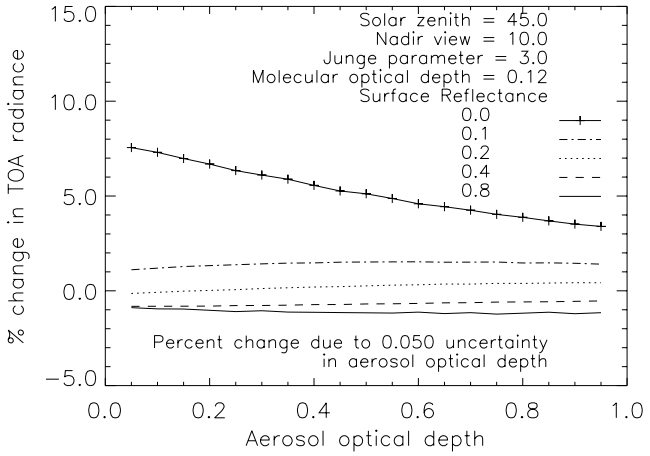

Figure 10 Uncertainty in TOA radiance due to an 0.05 change in aerosol scattering optical depth

3.1.3.d Junge parameter

To examine the effects of incorrectly estimating the Junge size distribution parameter, the same basic case as used to study the effects of optical depth was used. In addition, further RTC runs were made with Junge parameters of 2.0, 2.5, 3.5, and 4.0. The percent change in TOA radiance due to a 0.5 error in Junge parameter is shown as a function of reflectance for several optical depths in Figure 13. For clarity, only the case for a Junge parameter of 3.0 is presented in this figure. As can be seen, the effects of errors in the Junge parameter depend heavily on both the optical depth and the surface reflectance, with the largest errors for cases of low reflectance and high optical depths.

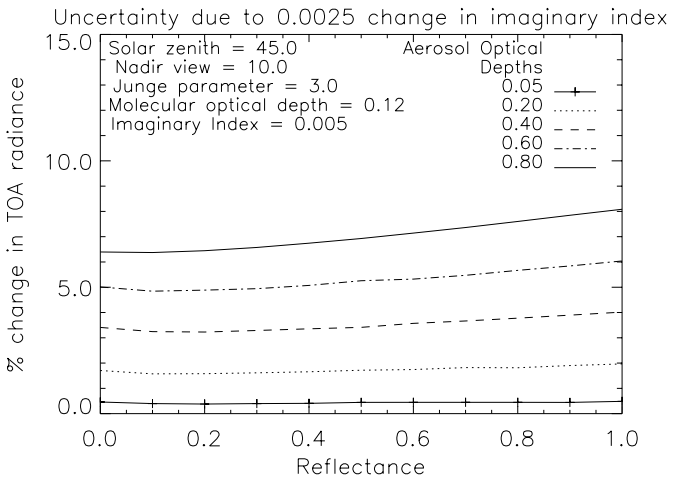

Figure 11 Uncertainty in TOA radiance due to an 0.0025 change in complex index of refraction

Figure 14 presents the results for a surface reflectance of 0.1 for each of the Junge parameters as a function of optical depth. From this figure it can be seen that errors are largest for larger values of the Junge parameter.

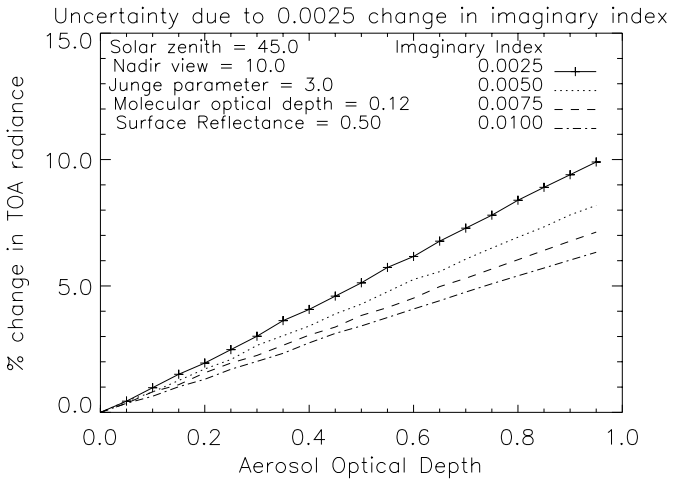

Figure 12 Uncertainty in TOA radiance due to an 0.0025 change in complex index of refraction

A much larger possible error can be the assumption of a Junge size distribution when this size distribution is not appropriate. King et al. (1978) and Hart (1990) investigated the inversion of spectral optical depths to obtain the aerosol size distribution. Hart finds as high as a 3.6% change in TOA radiance and as low as 0.2% for conditions at White Sands Missile Range. This uncertainty is difficult to quantify and is thus ignored in this error analysis. It should be kept in mind though that this error is present.

3.1.3.e RTC accuracy and LUT

The LUT line in the table shows the largest expected uncertainty in computing the radiance using the LUT. If this value is exceeded, the LUT will be modified to reduce the uncertainty.

The authors of the radiative transfer code used here claim an inherent code accuracy of no worse than 1%. Comparisons between independent codes making similar assumptions (Mie scattering by the aerosols, Junge size distributions, etc) but different numerical techniques, give results which compare at the 1% level.

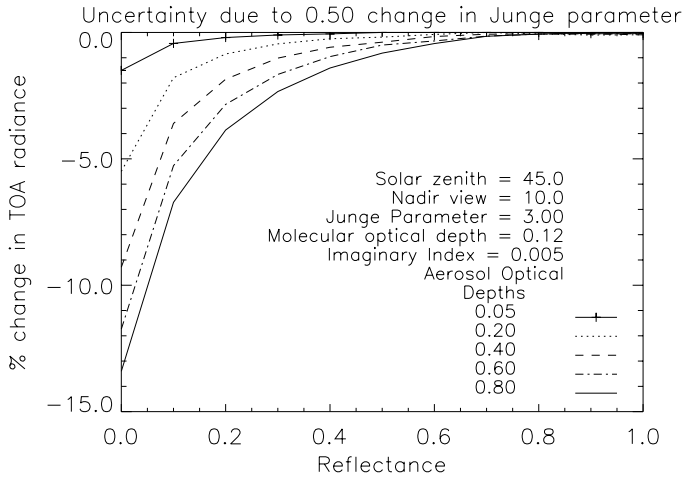

Figure 13 Uncertainty in TOA radiance due to an 0.5 change in the Junge size distribution parameter

<u>3.1.3.f Surface height and slope</u>

Since the surface elevation will be used to adjust the scattering optical depths, there will be uncertainties due to the surface height derived from the input DEM. To examine this uncertainty, the same base case used above was used and run for a surface elevation of 0 m. The molecular and scattering optical depths were then reduced to correspond to value which would be seen at 100 m based upon the vertical profile of scatterers in the standard model atmosphere used in the RTC. The results depend heavily upon the surface reflectance and the total scattering optical depth, with the largest errors occurring at low reflectance and large optical depths. For the low reflectance case, the error is approximately 4% and for the high reflectance case it is <1%.

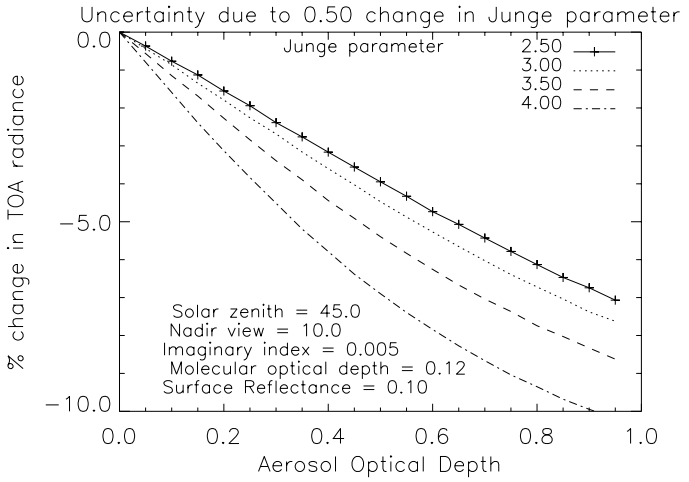

Figure 14 Uncertainty in TOA radiance due to an 0.5 change in Junge size distribution parameter

Uncertainty due to surface slope has not been included in either table because it is not possible to assess this using the current RTC. In retrieving the surface radiance we will not attempt to account for surface slope effects because this would make the LUT prohibitively large. We will use surface slope to adjust the retrieved surface reflectance. Since this will be a simple cosine correction, the uncertainty in retrieved surface reflectance will be related to the cosine of the slope angle of the surface. Thus, for a given slope error, the error in surface reflectance will be much larger as the slope angle increases. A five degree error in slope at 30 degrees gives a five percent error in surface reflectance. The same five degree error at a slope angle of 45 degrees is eight percent. It should be noted that, since the

RTC assumes a plane parallel earth-atmosphere system, as the slope angle increases, so will uncertainties in the RTC results.

3.1.3.g Surface BRF

The LUT being generated for the atmospheric correction assumes the surface to be lambertian. This has been done for two reasons, the first is that to include BRF effects in the LUT would make the table prohibitively large. The second is that there will be no BRF information available at the 30-m scale which could be used for the atmospheric correction. To understand the effects caused by assuming a lambertian surface, the radiative transfer code was run for a number of different surface BRFs.

Case 1 used a surface which had a factor of 10 greater reflectance factor for angles within 30 degrees of the horizon than for the nadir hemispherical-direct value. Case 2 simulated a hotspot effect with the reflectance factor in the backscatter direction being a factor of 2 greater than that for the nadir hemispherical-direct value. For these two cases, the solar angle was 45 degrees, thus, BRF effects only manifested themselves in the multiply-scattered radiance at the sensor. Case 3 was identical to Case 2 except the sun angle was assumed to be 18 degrees and thus, the hotspot was viewed directly.

Using these cases, plus the lambertian case, the RTC was run for a variety of hemispherical-directional reflectances and aerosol optical depths. Aerosol absorption was assumed to be zero, the real index of refraction was 1.44, and the Junge parameter was 3.0. Satellite view nadir angles from 0 to 24 at two degree intervals were used as well as relative azimuths of 0, 90, and 180 degrees. The molecular optical depth was assumed to be 0.12, which corresponds to the value at sea level for band 1 of ASTER.

To compute the effect of BRF on the retrieved reflectance, the percent change in TOA radiances were determined between the lambertian and non-lambertian cases. For all three of the above described cases, the percent difference in radiance was less than 1%, except of course for the cases when the sensor would be directly viewing the hotspot. In this case, the reflectance derived from the non-lambertian radiances using a linear interpolation of the lambertian results gives an error of 4-7% at low optical depths. This error is larger at higher optical depths due to attenuation of the radiation from the hotspot.

One other effect which has not been examined yet is that due to specular reflection from water bodies. While the current radiative transfer code can use a non-lambertian surface, it does not treat specular reflection properly. The effect of specular reflection could be important for the ASTER-only atmospheric correction described earlier because a small change in the apparent reflectance of the water surface will seriously affect the retrieved aerosol parameters.

3.1.3.h Total estimated error

Based upon the above, the total uncertainty due to all of these components is 15% for the low reflectance case and 8% for the high reflectance case. This estimated error does not include the

effects of assuming a lambertian surface. It must also be reiterated that these uncertainties are only being used here to give the reader a feel for possible sources of uncertainty and levels, but they do not represent the actual values from ASTER. The error in the retrieved surface reflectance and surface radiance due to this will depend on the relationship between TOA radiance and surface reflectance and surface radiance. We used the results shown in Figure 1 to estimate the error in retrieved surface reflectance.

For the low surface reflectance case (Table 4), a 15% uncertainty in the radiance leads to an uncertainty in the surface reflectance of 30-70% from a true surface reflectance of 0.05 depending upon the total optical depth. This corresponds to between 0.016 and 0.035 units in reflectance. For the high surface reflectance case (Table 3), the 8% uncertainty leads to a 7-9% uncertainty in surface reflectance at a value of 0.5 for the true surface reflectance. This corresponds to between 0.037 and 0.043 units in surface reflectance.

It should be noted that the above values correspond well to those found when this approach was applied to TM (Holm et al., 1989) and HRV (Moran et al., 1990). These values are also similar in size to those found for several other atmospheric correction approaches (Moran et al., 1992). It should be heavily emphasized that the papers which have been cited all used ground-based measurements of atmospheric parameters, and thus represent what one would expect to be a best case. Thus, it is doubtful that using a more complicated atmospheric correction scheme will improve the uncertainties listed above, since it will be the uncertainty in the input parameters which is the largest source of uncertainty in the final result.

3.2 Practical Considerations

This section describes anticipated techniques for algorithm implementation. A detailed plan for implementation is not given here. This section focuses on the practical issues involved in algorithm implementation, including programming and procedural issues, validation, quality control, data dependencies, exception handling, and a description of the output product.

3.2.1 Implementation Plans

The software will be developed to allow for future upgrades. Currently, we are developing Version 1 of the code to be followed by two upgraded versions. We do not anticipate major algorithmic changes between this version and the final version because of the history of LUT approaches. This, however, does not preclude improvements as knowledge of the problem becomes greater. Some of the items for improvement include handling adjacency effects, surface slope, and lack of outside aerosol information. The detail with which each of these items is implemented will depend on the computational requirements of the Version 1 code. By knowing ahead of time that such possible upgrades are planned, the code can be developed to allow these modifications to be implemented without major rewrites.

3.2.2 Programming/Procedural Considerations

The primary programming effort in this project focuses on two separate issues. The first involves development of the LUT code to retrieve the surface reflectance and surface radiance. This programming effort is concentrated at the Jet Propulsion Laboratory (JPL) with input from RSG personnel. The second effort concentrates on the development of the code which generates the LUT itself. This work is occurring primarily at the RSG with help from JPL personnel to ensure the finished software will run properly on alternate platforms.

The atmospheric correction code is being developed in steps. This development began with a prototype implementation of the code to test the basic processing steps at the DAAC. In addition, early coding efforts developed software to store the LUT results in a database and software to retrieve these data from the database. The prototype implementation showed that several modifications are necessary to optimize the way in which the LUT is accessed from the database. The prototype was also used to ensure that the method of code development at JPL from algorithm specifications from the RSG proceeded in a satisfactory fashion.

The prototype code used only a limited version of the LUT. The version that will be used for Version 1 should closely match the size of the final table, but does not include the results of the LUT resolution study. Thus the Version 1 table will be different from the at-launch version.

3.2.3 Calibration and Validation

The validation approach is similar to past work (Holm et al., 1989) and is based upon the methods developed for the reflectance-based calibration described earlier (Slater et al., 1987). The field measurements will provide an opportunity to validate both the inputs to the atmospheric correction and the output products. It will be important to determine the uncertainties of the inputs to the atmospheric correction because, as shown in the sensitivity analysis, it is expected that these uncertainties will dominate the overall uncertainty. In the prelaunch phase of the validation, the climatological inputs will be validated. The post-launch work will continue to examine the climatological data sets as well as look at the uncertainties of the MODIS, MISR, and GAM products which will be used. Another reason to determine the input uncertainty effects on the output product, is this will allow us to reduce the number of field campaigns required.

3.2.3.a Test site selection and required measurements

The most difficult aspect of the validation is selecting appropriate test targets. Currently, all test sites used by the RSG are for vicarious calibration. As such, they are sites with high reflectance located in clear atmosphere regions. These sites could be used for the validation of the atmospheric correction of ASTER, but they would not provide much information about the accuracy of the algorithm.

Recall that the bands of interest are the VNIR and SWIR which have ground-spatial resolutions of 15 and 30 m respectively. Two criteria will be applied to the test targets to minimize the effects of

sampling. The first is targets should be homogeneous over at least a 45-m × 45-m area. This ensures the pixel we use in the ASTER image will be a "pure" pixel. The second criteria defines what is meant by "homogeneous." The average of the measured reflectance of the target must not vary by more than 0.005 in reflectance units when the sampling by the ground-based spectroradiometer is changed. Ideally, the site should have a high probability of cloudless skies to increase the chance of successful field campaigns, easy access, and proximity to the RSG (to reduce travel costs).

To completely study the problem, requires test sites which satisfy a wide range of surface reflectances, surface relief, horizontally varying surface reflectance, different aerosol types, a range of aerosol concentrations, and varying amounts of absorbing gases. If the extremes are selected, this leads to validation sites which have combinations of

1) Low and high aerosol optical depths
2) Two different aerosol types (marine and continental, for example)
3) Low and high humidities
4) Dark and bright surfaces
5) Flat and highly-sloped surfaces
6) Horizontally-homogeneous surface and one with widely varying reflectance
7) Clear-sky and thin-cloud cases

This would lead to a dizzying number of targets and require a large validation budget. Thus, a compromise is required. This compromise is to select targets which first ensure the algorithm operates properly for simplistic cases. Theoretical data are then used to predict cases for which the algorithm might have difficulties and select targets to evaluate these predicted problem areas. An example of how this might work would be to select a flat, homogeneous, dark target in a turbid atmosphere. If the algorithm is successful in this case, the algorithm is used as part of a sensitivity analysis to determine what conditions are likely to cause problems. While this approach does not experimentally test all cases, it makes good use of available resources.

A single target will be used as a primary validation site. This primary target should have several areas of at least 45 m × 45 m in size with uniform reflectance and each area having a different value of surface reflectance. The target area should have moderate levels of turbidity (aerosol optical depths > 0.30) and preferably a possibility of both continental and marine aerosols. Since it is hoped the site can be within a one-day drive from Tucson, Arizona, the most likely candidates will be along the California coast. At this time, no specific targets have been selected. The prelaunch time frame will be used to evaluate possible targets for post-launch validation and we hope a coordinated selection can be made with inputs from other AM-1 sensor teams.

The number of validation sites being supported by ASTER can also be decreased through cooperative data collections with other validation groups. The only requirement is that these field campaigns must have surface reflectance data. It is also better if the data sets include atmospheric measurements, but these are not the critical data. No plans have been made to use any of the operational surface networks. The primary reason for this is the lack of surface reflectance data. For example, the DOE

ARM CART site is an excellent resource for information regarding atmospheric composition. It does not have information about the surface reflectance and thus cannot be used to validate this algorithm.

The measurements for the validation approach described below are in three categories: essential, desirable, and optional. There are two essential pieces of information. These are the surface reflectance of a selected test target and the location of this target. Without these data, a validation cannot be done. Desirable data are the characteristics of atmospheric aerosols and columnar amounts of gaseous absorbers. Without any of these data, the validation will rely on climatological values. This is still a useful validation, but is not as important as those which include more realistic inputs to the algorithm. There are two pathways with which the aerosol and gaseous absorber information can be obtained, ground-based measurements and satellite-derived values. Both are important to the overall validation plan, but only one is truly needed to perform a single validation. Ideally, both would be available. Optional data consists of additional atmospheric data. These would include sky radiance measurements used to derive scattering phase functions, downwelling diffuse and global irradiance, or surface meteorological data. These data are helpful in this validation work but are not essential.

3.2.3.b Validation criteria and measures of success

Successful validation of the algorithm occurs when the retrieved reflectance/radiance from ground-based methods agrees with the value retrieved by the algorithm to within the uncertainties of the two methods. The level of agreement will be site dependent because uncertainties are a function of the surface reflectance of the target and the atmospheric conditions.

3.2.3.c Prelaunch validation

Prelaunch validation activities are divided into two parts, theoretical and experimental. The theoretical validation uses test data sets to check the algorithm's sensitivity to a wide range of simulated atmospheric conditions. These tests will examine effects of input parameter uncertainties and LUT resolution. The test data sets are generated by converting surface reflectance to surface and TOA radiance using the same RTC used to generate the LUT. The experimental validation uses data sets from past field campaigns as well as from planned prelaunch field campaigns. The data sets consist of measured surface reflectance of selected test sites and ground-based solar radiometer measurements.

The prelaunch theoretical studies follow the same philosophy as that of the sensitivity and uncertainty analysis shown above. This work focuses on understanding what the output uncertainties of the algorithm are for a given input uncertainty. Understanding this effect will allow the output product uncertainty to be determined once the input uncertainties and values are known. This work will also point out the most sensitive cases which should be the focus of experimental, validation efforts.

For example, the sensitivity analysis discussed earlier shows effects of imaginary index are not strongly dependent upon surface reflectance. Thus, finding a specific surface target is not as critical as finding a high turbidity site with varying aerosol type. The results also show greater uncertainties

for cases of high Junge parameter, or equivalently, the aerosols are dominated by small-sized particles. This implies the validation site selected should sample this type of aerosol. The optical depth studies indicate more knowledge about the atmospheric correction's accuracy is obtained by studying a low-reflectance target (reflectance less than about 0.1). This implies that high-reflectance targets are not critical to understanding the accuracy of the atmospheric correction. These conclusions allow a more focused search for candidate sites and reduces the number of targets which are needed.

The sensitivity study also indicates that finding methods for determining the aerosol size distribution and complex index of refraction will be critical to the validation work. This has led to the RSG developing new instrumentation which should be available for the validation of the atmospheric correction. This includes a system to measure the downwelling diffuse irradiance and another system which will be used to measure the solar aureole.

Also included in prelaunch validation will be a comparison of results obtained by different RTCs to quantify the accuracy of the code used in the LUT generation. The uncertainty/sensitivity analysis will examine effects from the LUT including the parameterization the aerosols into a format suitable for using the LUT and effects due to the discrete nature of the LUT.

In addition to prelaunch theoretical studies, there will also be prelaunch experimental work. This experimental work will serve three primary purposes: 1) validation methodology tests; 2) test site evaluation; and 3) algorithm testing. Validation methodology tests mean prelaunch field campaigns will be used to practice techniques needed in the post-launch era. Test site evaluation will be used in the prelaunch time frame to help select the one or two primary sites which will be used for the post-launch algorithm validation. Finally, the prelaunch experiments will be used to determine any major flaws in the algorithm so that it can be changed before the post-launch version is delivered to the DAAC. The experimental approach for prelaunch validation is identical to the approach for the post-launch validation described later.

The prelaunch validation will also use the large number of currently existing data sets, such as the FIFE data. These data sets consist of coincident ground-, aircraft-, and satellite-based data which are ideally suited for the prelaunch validation of this algorithm. This work will focus on those portions of the data sets which have high-spatial resolution VNIR and SWIR data. The preferred satellite data is Landsat-5 Thematic Mapper or AVIRIS because both have bands in VNIR and SWIR. The key point is this work can use only those images for which ground-based atmospheric and surface reflectance data exist at the time of overpass.

3.2.3.d Post-launch validation

The post-launch validation plan is very similar to the prelaunch, with both experimental and theoretical studies. The plan for the post-launch validation is to focus efforts during the first six months of the sensor's time in orbit. These early efforts must be considered carefully because this is the time during which the sensor is expected to change most rapidly. It would not be productive to plan a validation campaign if the uncertainty in the sensor radiance dominates the retrieval of

surface reflectance and surface radiance. Once the sensor has stabilized to a point where the calibration of the system is not the dominating uncertainty, several validation campaigns will occur. The goal will be to collect three data sets of the same target under similar atmospheric conditions that will be processed and used to assess the algorithm's accuracy.

The data will also be used to modify the algorithm if needed. These modifications will not occur until the next delivery of the post-launch code. Thus this first set of validation campaigns will be used primarily to determine algorithm accuracy.

The basic approach to the field validation is to measure the surface and atmosphere at the time of sensor overpass. The surface reflectance of the site is found by comparing radiometer measurements of the site to those from a panel of known reflectance. This known reflectance is found by calibrating the panel at RSG facilities using a pressed polytetrafluoroethylene standard by measuring the reflected radiance from the panel and standard at a variety of wavelengths and illumination angles. We use a value for directional, hemispheric reflectance of the standard provided by the National Institute of Standards and Technology. Polynomial fits are made to the measured data to calculate the reflectance of the barium sulfate for the sun-view geometry and wavelengths for a given set of field measurements (Biggar et al., 1988).

Field measurements are made by carrying a spectroradiometer across the entire site. The radiometer has bands in both the VNIR and SWIR. The instrument is transported across the site by attaching it to a backpack device, or yoke, which extends the instrument away from the body of the user. The user collects at least 10 reflectance samples along a straight-line path within the area representing an ASTER SWIR pixel. Reflectance of the site is determined by comparing measurements of the site to those of the calibrated panel and averaging all of the measurements. Sun-angle changes and the bi-directional reflectance of the reflectance panel are taken into account when determining the reflectance. Global irradiance data are used to determine the significance of changes in diffuse skylight illumination.

Atmospheric measurements rely primarily on solar radiometers. We use two solar radiometers, one with ten bands and the other with three. Data from the ten-band radiometer are used in a Langley method retrieval scheme to determine spectral-atmospheric optical depths (Gellman et al., 1991). The radiometer is relatively calibrated immediately prior to, during, or after each field campaign. The optical depth results are used as part of an inversion scheme developed by the RSG to determine ozone optical depth and a Junge aerosol size distribution parameter (Biggar et al., 1990). The size distribution and columnar ozone are used to determine the optical depths at the wavelengths of the ASTER bands in the VNIR and SWIR.

The three-band radiometer is designed for columnar water vapor retrieval (Thome et al., 1994) using a modified Langley approach (Thome et al., 1992). Here, as for the optical depth retrieval, the primary uncertainty in water vapor is the instrument calibration and the system is calibrated prior to, during, or immediately after each campaign. The retrieved columnar water vapor is used in MODTRAN to determine band-integrated transmittances for ASTER wavelengths for the sun-to-surface-to-satellite path.

The surface reflectance and atmospheric data are collected at the selected test site at the time of an ASTER overpass. The ASTER data are then atmospherically corrected to surface radiance and surface reflectance in two ways. The first is the normal processing path of using satellite-derived inputs. The second replaces the satellite-derived inputs with the results of the ground-based, atmospheric measurements. Both sets of atmospherically corrected surface reflectance and radiance are compared to the ground-based surface reflectance and radiance measurements to determine the level of agreement. The results of the comparisons are then used to evaluate the success or failure of the algorithm and the role of input uncertainties.

3.2.3.e Validation example

Data collected by the RSG during a vicarious calibration at White Sands can be used as an example to illustrate the validation approach. Reflectance data were collected for an area equivalent to 64 Landsat-5 TM pixels on October 8, 1994 using a filtered spectroradiometer. The surface reflectance data were collected over a 40-minute period centered about the TM overpass by referencing to a field reflectance standard as described above. The reflectances computed at the wavelengths of the filtered radiometer were used in a spline fit routine to determine the reflectance for the bands of TM.

Solar radiometer data were collected during this same time period using the RSG's 10-band manual solar radiometer. Atmospheric optical depths were computed from these data for the 10-minute average around the overpass time and used to determine a Junge parameter related to the aerosol size distribution and a columnar ozone amount. These quantities were used to compute the atmospheric optical depths for the TM wavelengths. The optical depths and size distribution were used as inputs to the Gauss-Seidel iteration RTC for surface reflectance values of 0.4 and 0.5. The RTC results give the at-sensor radiance for the altitude of TM for each band.

The DN values for the 64 pixel area, marked in the image by tarpaulins laid at all four corners of the site, were converted to radiance using the calibration coefficients for TM. These radiances were then converted to surface reflectance using the RTC results for the two surface reflectances and assuming a linear relationship between at-sensor radiance and surface reflectance. The RTC-derived results using the TM imagery can be compared to the values measured at the surface. For this case, 3×3 pixel areas of the ground-based and image-based reflectances were averaged for the comparisons. This averaging reduces effects of misregistration of the ground-based data to the imagery. When the 3×3 pixel average reflectances for band 2 of TM were compared, the absolute difference between the image-based and ground-based reflectances differed by less than 0.01. The difference between the average reflectances for all 64 pixels was found to be less than 0.002. Of course, this excellent agreement is to be expected since the calibration coefficients for TM were computed using the reflectance-based calibration approach. That is, the same surface reflectance data and radiative transfer code used to determine the sensor radiances were used in the atmospheric correction example. For the validation of ASTER data, an independent calibration will be used. Even though the calibration and validation in this example are not independent, the example still illustrates the approach that will be used.

3.2.3.f Implementation of validation results

The results of the validation campaigns will be used in two ways. The first will be to refine uncertainty estimates reported with the data product. These uncertainties will be developed during the prelaunch phase using the theoretical data sets described above. Once experimental data are obtained, the uncertainties will almost certainly require some changes. This could be in two fashions. The first would be to simply adjust the values of the reported uncertainties. The second is to use the validation results to indicate areas where the algorithm should be revised. As an example, the validation data could indicate the treatment of surface slope effects causes uncertainties which could be reduced by changing the algorithm. Whether the algorithm is actually modified depends on the anticipated change in uncertainty, the complexity and computational requirements of the change, and cost to implement the algorithm change.

The second way validation results will be used is to determine the primary sources of uncertainty. There are two approaches to validation, the first is to simply see how well the final product is retrieved and assess its uncertainty. This is described in the previous paragraph. The second approach evaluates the input parameters and algorithm. This is the purpose of the ground-based measurement of atmospheric properties. These can be used to evaluate the accuracy of the inputs to the algorithm, in essence validate the inputs. The goal of this portion of the validation will not be to force changes in how the input data are produced. Instead, it is to identify unsuitable inputs, determine which parameterizations of the inputs affect the results, create uncertainty estimates which are a function of input type and value, and evaluate other ways to use input data sets through algorithm modification.

3.2.3.g Archival of validation data

Archival of the validation data will be done at RSG facilities. The data will be archived in raw and processed format on Sun-based hard disks and 8-mm tapes using UNIX tar commands. Distribution of the data will be through ftp access. A word-wide web site is currently being developed for the RSG. This site will be used to allow others to see a list of available data, samples of the data, and summaries of the results. The site will also instruct users how to retrieve copies of the data from the ftp site.

3.2.4 Quality Control and Diagnostics

Quality control and diagnostics will be developed to inform the end user of the uncertainties expected in the final results. This includes addressing the effects of sub-pixel clouds and adjacent clouds. We anticipate that a cloud mask routine will be supplied to this algorithm that allows the uncertainty reported with the quality assessment (QA) to be adjusted accordingly when clouds are present. This information, as well as the information indicating the accuracy of the required input parameters, will be used to inform the end user of the quality of the results.

Diagnostics will be implemented to flag results which are not physically plausible, such as reflectance greater than 1 or less than zero. In these cases, the scene will be manually inspected to determine if

the atmospheric correction broke down, the satellite data are bad, or some other cause. A certain number of scenes will be manually inspected to determine if the atmospheric correction is behaving as expected.

3.2.5 Exception Handling

In cases when no ASTER data are available for some pixels either due to saturation or data dropouts, no retrieved surface reflectance or surface radiance will be reported. The user will be informed of these pixels through a QA image supplied with the output of the algorithm.

A more important case to consider is when outside data are not available. In these cases, secondary sources for the information will be accessed until all possible sources have been exhausted. When this occurs, climatological data will be used. Thus, whenever valid ASTER data for a pixel are present, there will be a retrieved surface reflectance and radiance. These reported values will have the appropriate uncertainties associated with them, with increasing uncertainty as more secondary data sources are used.

3.2.6 Data Dependencies

There are several data dependencies for this algorithm. Figure 15 shows a data flow diagram for the atmospheric correction. In this figure all dashed lines indicate data which must be obtained from sources outside of the ASTER data stream. Data included within the ASTER data stream are instrument view angle, satellite and solar zenith angles, and the ASTER TOA radiances. The rounded boxes indicate processes which act upon the data. Open rectangles indicate data files. The

LUT is represented by the LUT Radiances open rectangle. It is generated by the RTC represented by process 7. This process obtains the RTC parameters necessary to generate the table from the LUT Parameters data file. Processes 1, 2, and 3 can be considered as pre-processing steps to the actual atmospheric correction which occurs in processes 4, 5, and 6.

The current planned sources for outside data are as follows. The inputs to process 1 are surface pressure, band-absorption model data, filter profiles, absorption-model atmospheres, and columnar-absorbing gases. Surface pressure will be used to compute the carbon dioxide and oxygen gaseous transmittances. This can be obtained approximately from the surface elevation based on climatology or can be obtained from the same source used by the MODIS and MISR Science teams. The band-absorption model data and the absorption-model atmospheres are used to compute the band-integrated transmittances based on the supplied filter profiles and the columnar amount of the absorbing gas, either water vapor or ozone. The filter profiles must be obtained from the manufacturer of the VNIR and SWIR sensors of ASTER. The information related to the absorption

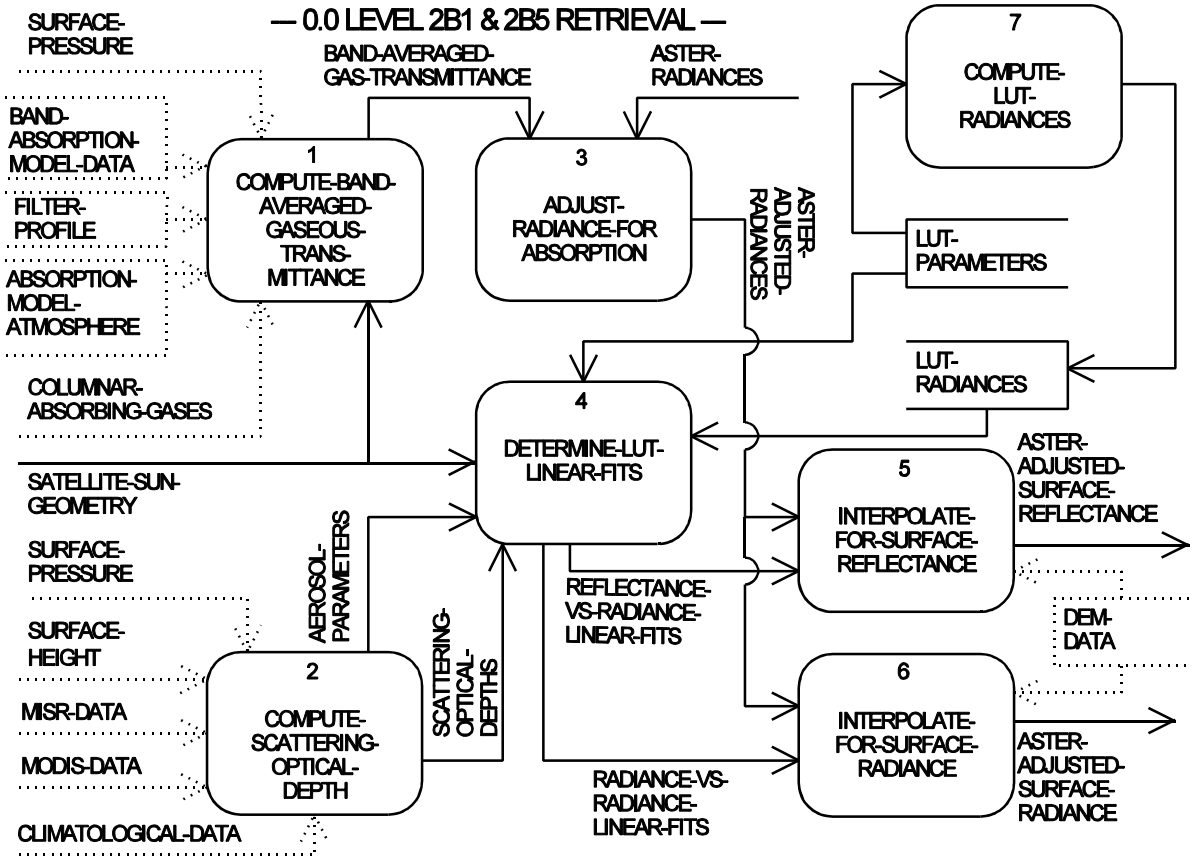

Figure 15 Data flow diagram for the ASTER Level 2B1 surface radiance and Level 2B5 surface reflectance retrievals.

model and the columnar amounts will be obtained from the same source as used by the TIR atmospheric correction to maintain internal consistency. Possible sources of the columnar amounts are GAM or MODIS results. The most likely source of the band-model data is MODTRAN/LOWTRAN.

The inputs to process 2 are surface pressure and height, MISR data, MODIS data, and climatology. All of these input variables are used to determine the scattering optical depths at the ASTER band-center wavelengths. The surface pressure will be obtained as described above. The surface height must be obtained from a DEM. MISR data refer to the aerosol products to be produced by the MISR Science Team, specifically aerosol size distribution and single scatter albedo. If no aerosol size distribution is available, a derived distribution based on the aerosol optical depths will be found. If no MISR data are available, we will rely on MODIS derived aerosol parameters in a similar fashion. If no MISR or MODIS data are available then climatologically derived values are intended to be used. At a later date, process 2 will be revised to allow the calculation of the needed aerosol parameters using ASTER data alone.

The only other scene-dependent outside data required for this algorithm are DEM derived surface slopes and heights. The intended use of the slope is for performing a slope correction to the surface reflectance. The intended use of the height is to adjust the scattering optical depths for elevation.

Figure 16 shows the ASTER product interdependencies and the relationship of the atmospheric correction to the other products that will be produced by ASTER. From this diagram it can be seen that the ASTER data used by the surface reflectance and radiance retrieval require data from the DEM database and uses calibrated, registered radiances from the VNIR and SWIR telescopes. The results of the atmospheric correction are in turn used to refine the cloud classification.

3.2.7 Output Product

The output products of this algorithm are surface reflectance and surface radiance. Both will be reported as real numbers with a precision that does not exceed the estimated accuracy. Accompanying each product will be a summary of the input parameters used to derive the reported surface reflectance and radiance. Also included will be uncertainty estimates and a description of the algorithm.

4.0 CONSTRAINTS, LIMITATIONS, AND ASSUMPTIONS

Constraints, limitations, and assumptions can be broken into four sections. The first relates to the RTC used to generate the LUT, the second to the determination of aerosol optical depths at the ASTER wavelengths, the third to the actual look-up approach, and the fourth to the radiometric changes that the sensor itself introduces into the image. The reader should always keep in mind that the atmospheric correction can always be applied to any scene. Thus there are no limits to the application of this algorithm. However, the accuracy of the results can be severely reduced if the assumptions made in the method are not valid.

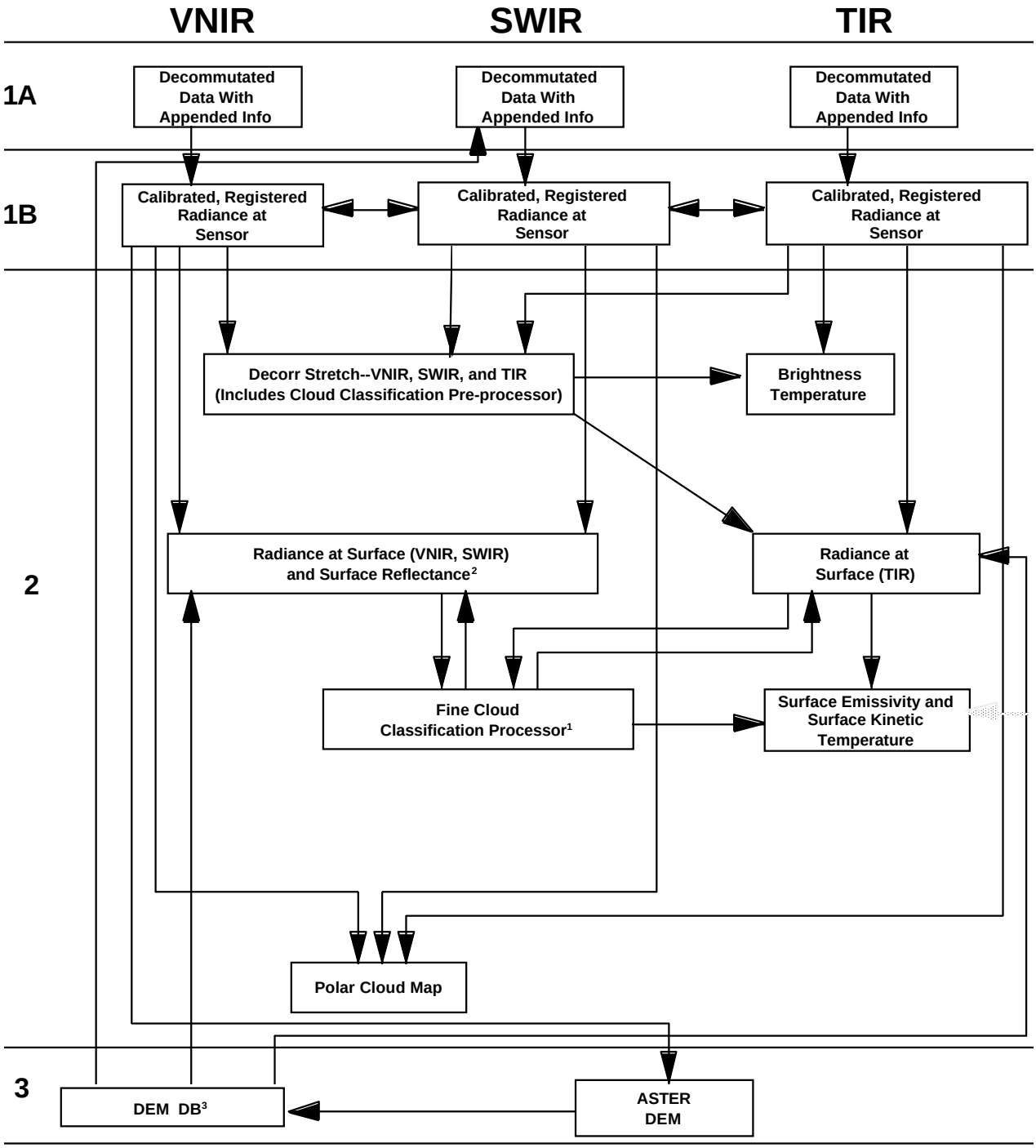

[1]Produces a cloud mask that is incorporated into other products
[2]Computed simultaneously with Radiance at Surface
[3]Refers to a database of DEM data regardless of the source

Figure 16. Figure showing ASTER product inter-dependencies.

The RTC assumes the atmosphere follows the 1976 US Standard atmosphere with a modification for stratospheric aerosols. It also assumes the atmosphere is plane-parallel and homogeneous and the aerosols scatter as Mie particles with assumed values for the refractive index. This particular radiative transfer model can only be used in cases where the atmosphere is relatively horizontally homogeneous. This precludes using the model in the presence of clouds in most cases. Cirrus clouds are treated as aerosol scatterers but not as layers. Volcanic aerosols are treated by modifying the vertical distribution of aerosols, but a new LUT has to be generated in this case.

The method for determining aerosol scattering optical depth assumes the aerosol size distribution follows a Junge power law and gives the Junge size distribution which best fits the measured optical depths. For most earth atmosphere situations, this is an adequate assumption. Because the assumption greatly simplifies the LUT, alternate size distributions are not planned to be used.

The greatest assumption in the LUT determination of the surface reflectance and surface radiance is that a linear relationship exits between these parameters and the TOA radiance over a selected range of reflectance. This will not be a limitation to the applicability of the method because we will develop the table to account for this.

Every sensor introduces radiometric errors into the images it produces. These errors can be divided into two categories, those anticipated when the performance specifications are written and those that only show themselves when the sensor is being carefully characterized. MTF effects fall into the former category. These give rise to an increasing error as the size of image detail decreases. It is possible to perform an MTF inversion on the image to reduce the MTF effect, however, this is quite computer intensive. Various other, sometimes unanticipated, effects can reduce the radiometric fidelity of the image and many of these are image-contrast dependent. Examples are: the memory effect, stray light, polarization, and errors due to non-linearities and imprecise knowledge of the sensor's spectral responses. Without correction, these effects can produce errors in the neighborhood of 5% and, in some cases, depending on the size and contrast of the image structure, considerably more. To reduce the magnitude of these effects the sensor performance has to be carefully quantified and correction algorithms implemented. It is not anticipated that such algorithms will be formulated until the results of preflight characterizations of the ASTER sensors have been conducted.

5.0 REFERENCES

Biggar, S. F., D. I. Gellman, and P. N. Slater, "Improved evaluation of optical depth components from Langley plot data," *Rem. Sens. Env.* **32**:91-101, 1990.

Bohren, C. F., and D. R. Huffman, *Absorption and Scattering of Light by Small Particles*, (John Wiley and Sons, New York), pp. 475-482, 1983.

Fraser, R. S., O. P. Bahethi, and A. H. Al-Abbas, "The effect of the atmosphere on the classification of satellite observations to identify surface features," *Rem. Sens. Env.*, **6**:229-249, 1977.

Fraser, R. S, R. A. Ferrare, Y. J. Kaufman, B. L. Markham, S. Mattoo, "Algorithm for atmospheric correction of aircraft and satellite imagery," *Int'l. J. Rem. Sens.*, **13**:541-557, 1992.

Fraser, "Atmospheric corrections for ocean color," Presented at the Remote Sensing of Aerosol from MODIS and EOS and Atmospheric Corrections Workshop, Greenbelt, Maryland, May 17-18, 1993.

Gellman, D. I., Biggar, S. F., Slater, P. N. and Bruegge, C. J., "Calibrated intercepts for solar radiometers used in remote sensor calibration," *Proc. SPIE* **1493**:175-180, 1991.

Gellman, D. I., S. F. Biggar, M. C. Dinguirard, P. J. Henry, M. S. Moran, K. J. Thome, and P. N. Slater, "Review of SPOT-1 and -2 calibrations at White Sands from launch to the present," *Proc. SPIE*, **1938**, 1993.

Hart, Q. J., *Surface and aerosol models for use in radiative transfer codes*, M.S. Thesis, University of Arizona, 66 pp., 1990.

Herman, B. M. and S. R. Browning, "A numerical solution to the equation of radiative transfer," *J. Atmos. Sci.*, **22**:559-566, 1965.

Holm, R. G., R. D. Jackson, B. Yuan, M. S. Moran, P. N. Slater, and S. F. Biggar, 1989, "Surface reflectance factor retrieval from Thematic Mapper data," *Rem. Sens. Env.*, **27**:47-57.

Kahle, A.B., F.D. Palluconi, S.J. Hook, V.J. Realmuto, G. Bothwell, "The Advanced Spaceborne Thermal Emission and Reflectance Radiometer (ASTER)," *Int'l. J. Imaging Systems and Tech.*, Vol. 3, pp. 144-156, 1991.

Kaufman, Y. J., "The atmospheric effect on the separability of field classes measured from satellites," *Rem. Sens. Env.*, **18**:21-34, 1985.

Kaufman, Y. J. and C. Sendra, "Algorithm for automatic atmospheric corrections to visible and near-IR satellite imagery," *Int'l. Journal Rem. Sens.*, **8:**1357-1381.

Kimes, D. S., and P. J. Sellers, "Inferring hemispherical reflectance of the Earth's surface for global energy budgets from remotely sensed nadir or directional radiance values," *Rem. Sens. Env.*, **18**:205-223, 1985.

King, M. D., D. M. Byrne, B. M. Herman, and J. A. Reagan, "Aerosol size distributions obtained by inversion of spectral optical depth measurements," *J. Atmos. Sci.* **35**:2153-2167, 1978.

Moran, M. S., R. D. Jackson, G. F. Hart, P. N. Slater, R. J. Bartell, S. F. Biggar, D. I. Gellman, and R. P. Santer, "Obtaining surface reflectance factors from atmospheric and view angle corrected SPOT-1 HRV data," *Rem. Sens. Env.*, **32**:203-214, 1990.

Moran, M. S., R. D. Jackson, P. N. Slater, and P. M. Teillet, "Evaluation of simplified procedures for retrieval of land surface reflectance factors from satellite sensor output," *Remote Sens. Environ.*, **41**:169-184, 1992.

Richter, R., " A fast atmospheric correction algorithm applied to Landsat TM images," *Int'l. Journal of Rem. Sens.*, **11**:159-166, 1990.

Slater, P. N, S. F. Biggar, R. G. Holm, R. D. Jackson, Y. Mao, M. S. Moran, J. M. Palmer, and B. Yuan, "Reflectance- and radiance-based methods for the in-flight absolute calibration of multispectral sensors," *Rem. Sens. Env.*, **22**:11-37, 1987.

Slater, P. N. and R. D. Jackson, 1982, "Atmospheric effects on radiation reflected from soil and vegetation as measured by orbital sensors using various scanning directions," *Appl. Opt.*, **21**:3923-3931.

Stowe, L., "NOAA/AVHRR aerosol optical thicknessproduct team," Presented at the Remote Sensing of Aerosol from MODIS and EOS and Atmospheric Corrections Workshop, Greenbelt, Maryland, May 17-18, 1993.

Takashima, T. and K. Masuda, "Simulation of atmospheric effects on the emergent radiation over a checkerboard type of terrain, *Astrophy. Space Sci.*, vol. 198, pp. 253-263, 1992.

Takashima, T. and K. Masuda, "Operational procedure of atmospheric correction on satellite visible data allowing for the adjacency effect," *Proc. of SPIE*, 1996, **2817**:70-81, 1996.

Tanre, D., M. Herman, and P. Y. Deschamps, "Influence of the background contribution upon space measurements of ground reflectance," *Appl.Opt.*, **20**:3676-3684,1981.

Teillet, P. M., "An algorithm for the radiometric and atmospheric correction of AVHRR data in the solar reflective," *Rem. Sens. Env.*, **41**:185-195, 1992.

Thome, K. J., D. I. Gellman, R. J. Parada, S. F. Biggar, P. N. Slater, and M. S. Moran, "In-flight radiometric calibration of Landsat-5 Thematic Mapper from 1984 to present," *Proc. of SPIE*, **1938**, 1993.

Thome, K. J., B.M. Herman, and J.A. Reagan, "Determination of precipitable water from solar transmission," *J. of Appl. Met.*, **31**:157-165, 1992.

Yamaguchi, Y., H. Tsu, and H. Fujisada, "A scientific basis of ASTER instrument design," *Proc. SPIE*, Vol. 1939, pp. 150-160, 1993.

Young, A. T., "On the Rayleigh-scattering optical depth of the atmosphere," *J. Appl. Met.*, **20**:328-330, 1981.

APPENDIXES

A. List of Acronyms

ASTER	Advanced Spaceborne Thermal Emission and Reflectance radiometer
ATBD	Algorithm Theoretical Basis Document
BRF	Bidirectional Reflectance Factor
DAAC	Distributed Active Archive Center
DEM	Digital Elevation Model
DN	Digital Number
EOS	Earth Observing System
GAM	Global Assimilation Model
HRV	Haute Resolution Visible
JPL	Jet Propulsion Laboratory
MISR	Multi-angle Imaging SpectroRadiometer
MODIS	MODerate resolution Imaging Spectroradiometer
RTC	Radiative Transfer Code
RSG	Remote Sensing Group (of the Optical Sciences Center at the University of Arizona)
SPOT	Systeme Probatoire d'Observation de la Terre
SWIR	Short-Wave Infrared
TOA	Top-Of-Atmosphere
TIR	Thermal Infrared
TM	Thematic Mapper
VNIR	Visible, Near Infrared